SEL1L-HRD1 ER-associated degradation is a new ataxia gene

Liangguang Leo Lin[1]†, Mauricio Torres[1]†, Brent Pederson[1], Huilun Helen Wang[1], Xiaoqiong Wei[1], Zexin Jason Li[2], Xiaodan Liu[3,7], Hancheng Mao[1], Michalina Hanzel[4], Eve Ellen Govek[4], You Lu[1], Hui Wang[1], Mary Elizabeth Hatten[4], Zhen Zhao[3], Shengyi Sun[6*], Ling Qi[1,2,5*]

[1] Department of Molecular & Integrative Physiology,
[2] Department of Biological Chemistry, University of Michigan Medical School, Ann Arbor, MI 48105, USA
[3] Zilkha Neurogenetic Institute, Keck School of Medicine of University of Southern California, Los Angeles, CA 90033, USA
[4] Laboratory of Developmental Neurobiology, The Rockefeller University, New York, NY 10065, USA
[5] Division of Metabolism, Endocrinology & Diabetes, Department of Internal Medicine, University of Michigan Medical School, Ann Arbor, MI 48105, USA
[6] Center for Molecular Medicine and Genetics, Department of Biochemistry, Microbiology and Immunology, Wayne State University School of Medicine, Detroit, MI 48201, USA
[7] Present address: Department of Radiology and Biomedical Imaging, University of California San Francisco, San Francisco, CA 94143, USA
† Contribute equally
[*] Correspondence: lingq@med.umich.edu; shengyisun@wayne.edu

Running title: SEL1L-HRD1 ERAD in cerebellar ataxia

Keywords: SEL1L-HRD1 ERAD, disease variant knock-in mice, knockout mice, early-onset cerebellar ataxia, developmental delay, microcephaly, Purkinje cells, hypomorph, SEL1L-HRD1 interaction

One-sentence summary: Disruption of SEL1L-HRD1 interaction and function causes cerebellar ataxia in mice.

ABSTRACT

Despite recent advances in our understanding of the physiological importance of SEL1L-HRD1 endoplasmic reticulum (ER)-associated protein degradation (ERAD) using cell type-specific knockout (KO) mouse models, its relevance and importance in ataxia pathogenesis remain unknown. Here we show that loss of SEL1L-HRD1 ERAD complex interaction or function in Purkinje cells leads to cerebellar ataxia. Both homozygous knock-in (KI) mice carrying *SEL1L* variant *p.Ser658Pro* (S658P) and mice with Purkinje cell-specific deletion of SEL1L exhibit early-onset cerebellar ataxia, although disease severity and progression differ between the models. Structure-function analyses reveal that *SEL1L S658P* variant impairs, not abolishes, ERAD function by attenuating the interaction between SEL1L and HRD1. Proteomic screen of potential endogenous substrates leads to the identification of Astrotactin 1 and 2, two integral membrane proteins involved in neuronal function and development, whose maturation and biogenesis in the ER depend on SEL1L-HRD1 ERAD activity. These data demonstrate the pathophysiological importance of SEL1L-HRD1 interaction and function in the pathogenesis of cerebellar ataxia.

INTRODUCTION

A significant portion of secretory and membrane proteins entering the endoplasmic reticulum (ER) may fail to fold properly and are ultimately disposed of by a quality-control process known as ER-associated degradation (ERAD) (*1-3*). The suppressor of lin-12-like (SEL1L)- HMG-CoA reductase degradation 1 (HRD1) complex represents the most conserved branch of ERAD from yeast to humans (*4-6*). SEL1L is required for HRD1 protein stability and substrate recruitment (*4, 7, 8*), functioning as a scaffold for ERAD components such as OS9, ERLEC1, and degradation in ER (DERLIN) proteins (*8-16*). *In vivo*, SEL1L-HRD1 ERAD is indispensable for embryonic and adult development using germline- and inducible- knockout (KO) mouse models (*7, 17-19*). Subsequent studies using cell type-specific KO mouse models further demonstrated the vital importance of SEL1L and HRD1 in a cell type- and substrate-specific manner in many physiological processes including food intake, water balance, immune function, stem cell biology, and energy homeostasis (*2, 20-40*). For example, SEL1L-HRD1 ERAD in AVP and POMC neurons maintains systemic water balance and food intake by degrading misfolded prohormones ProAVP and POMC in the ER, thereby generating a conducive folding environment (*41, 42*). However, the importance of SEL1L-HRD1 ERAD in the pathogenesis of cerebellar ataxia remained largely unknown.

Cerebellar ataxia is a neurological disorder characterized by degeneration of the cerebellum and its associated structures, affecting motor control, balance, and coordination, leading to difficulties in walking, problems with fine motor skills, and speech (*43, 44*). Purkinje cells are a type of neuron found in the cerebellum and are characterized by their elaborate dendritic arbors (*45*). Dysfunction or degeneration of Purkinje cells can lead to a variety of diseases including cerebellar ataxia (*46*). Studies in both patients and model systems have implicated several dozens of cytosolic and nuclear proteins, including many ataxin proteins, in ataxia pathogenesis (*44, 47*). Moreover, heterozygous missense mutations in inositol 1,4,5-trispohosphate receptor type 1 (ITPR1), an ER calcium channel, have been identified in early onset, non-progressive, mild spinocerebellar ataxia type 29 (SCA29, OMIM #117360) by impairing calcium homeostasis in the ER (*48, 49*). Nonetheless, the importance of ER homeostasis and ER protein quality control mechanisms in ataxia pathogenesis remains largely unexplored.

In 2012, Kyostila et al. (*50*) reported the identification of a *SEL1L* variant *p.Ser658Pro* (c.1972T>C, NM_005065) in Finnish Hounds suffering from cerebellar ataxia. Although genetic analyses revealed a strong association between the variant and the disease (*50*), disease causality and systemic impact of the variant, as well as its underlying mechanism, remained to be established. Here, using knock-in (KI) mouse and cell models carrying *SEL1L p.Ser658Pro* variant as well as Purkinje cell-specific *Sel1L*-deficient mouse models, we provide unequivocal evidence that SEL1L-HRD1 interaction and function are required for Purkinje cell function/survival and play a key role in the pathogenesis of cerebellar ataxia.

RESULTS

Developmental delay of *Sel1L*^{S658P} KI mice

To establish the disease causality of *Sel1L*^{S658P} variant, we generated KI mice carrying this variant on the B6/SJL background using CRISPR/Cas9-based methods (fig. S1A). Two independent founders were established using PCR and sequencing (fig. S1, B and C) and then used to generate homozygous *Sel1L*^{S658P} KI mice. As similar results were obtained from each founder line, all results below were combined. KI mice exhibited modest growth retardation by ~10-15% in both sexes, starting at 3-4 weeks through the first 40 weeks of age (Fig. 1A). At 5 weeks of age, KI mice of both sexes were slightly shorter in body length compared to that of WT littermates (Fig. 1B). This growth delay was not due to reduced food intake or associated with abnormal blood glucose levels, as they were comparable among the cohorts (Fig. 1, C and D). Heterozygous mice for the variant appeared normal and healthy (Fig. 1, A to D), pointing to the recessive nature of the variant.

Much to our surprise, blind histological examination of peripheral tissues of 5-week-old KI mice by a pathologist revealed no obvious histological abnormalities in the pancreas, liver, kidneys, inguinal white adipose tissue (iWAT), and brown adipose tissue (BAT) (Fig. 1, E and F, and fig. S1D). Biochemical analyses of serum revealed no significant damage in the livers of both sexes based on the levels of alanine transaminase (ALT), alkaline phosphatase (ALP) and total

bilirubin (TBIL) (Fig. 1G), or in the kidneys based on blood urea nitrogen (BUN) and creatinine levels (CREA) (fig. S1E). Of note, although ALT level was significantly increased in male KI mice compared to that of WT littermates, it was still within the normal range (24.3-115.3 U/L) (Fig. 1G). Hence, these data demonstrate that *Sel1L*^{S658P} is a recessive hypomorphic mutation, causing growth retardation in mice.

Microcephaly of *Sel1L*^{S658P} KI mice

At 5 weeks of age, KI mice had reduced brain weight by ~10 % compared to those of age-matched WT and HET littermates (Fig. 2, A and B). Magnetic resonance imaging (MRI) analyses revealed smaller cerebellum and cortex in KI mice by ~10-15% relative to those of WT littermates, i.e. microcephaly (Fig. 2, C and D, and fig. S2A). Blind histological examination revealed no obvious histological abnormalities in various brain regions, including the cortex, of KI mice at 5-weeks of age (Fig. 2, E and F). Immunostaining of markers for neurons (NeuN, neuronal nuclei), astrocytes (GFAP, glial fibrillary acidic protein), and microglia (IbaI, ionized calcium-binding adaptor molecule 1) also showed comparable staining pattens in the whole brain or cortex of the two cohorts at 5 weeks of age (Fig. 2G and fig. S2B), excluding the possibility of massive cell death and neuroinflammation in KI mice. Hence, these data show that KI mice exhibit microcephaly with no massive cell death or inflammation in the brain.

Early-onset, non-progressive, mild ataxia in *Sel1L*^{S658P} KI mice

KI mice developed abnormal hind limb-clasping reflexes when suspended by their tails, starting at 3-9 weeks of age (Fig. 3, A and B). Intriguingly, the phenotype remained mild for up to 48 weeks of age, pointing to the non-progressive nature of the disease (Fig. 3, A. and B). In addition, unlike WT mice showing a normal symmetric gait characterized by the overlapping of hindlimb and forelimb paw prints, KI mice exhibited asymmetric gait patterns characterized by the lagging of the hindlimbs and reduction in stride length at 6 weeks of age (arrows, Fig. 3, C and D). Interestingly, while the balance beam test showed that KI mice at 6 and 12 weeks of age had no problems completing the test compared to WT littermates (Fig. 3E), some KI mice slipped and lost their balance while crossing the beam (Fig. 3F and Video S1), pointing to an impairment of balance. HET mice were comparable to WT littermates in all above tests (Fig. 3 and not shown), in line with the autosomal-recessive nature of the variant. These data show that

Sel1L^{S658P} KI mice exhibit growth retardation, microcephaly, and signs of early onset, non-progressive, mild ataxia, establishing the disease-causality and pathogenicity of this allele.

A mild reduction of Purkinje cells in *Sel1L*^{S658P} KI mice

To explore mechanistically how *Sel1L*^{S658P} causes early onset cerebellar ataxia in mice, we examined Purkinje cells in the cerebellum of KI mice as alterations in Purkinje cells are directly associated with cerebellar ataxia (*51-53*). Purkinje cells are arranged in a single layer in the cerebellar cortex, with their dendrites facing the molecular layer (ML) and their axons facing the white matter (WM) (Fig. 4, A and B). Quantitation of the number of Purkinje cells based on their unique location and morphology in H&E-stained sagittal sections of the cerebellum revealed a mild 15-20% reduction in KI mice at 5 weeks of age (Fig. 4, A and C). This reduction did not worsen with age as a similar level of reduction was observed at 24 weeks of age (Fig. 4, B and C). This result was further confirmed by the quantitation of the Purkinje cell marker Calbindin using Western blot (Fig. 4D) and immunostaining (Fig. 4, E and F). Cleaved caspase 3, a marker of apoptosis, was undetectable in the cerebellum of KI mice at either 5 or 24 weeks of age (Fig. 4G), suggesting that the reduction may not be due to elevated apoptosis. Hence, our data show that *Sel1L*^{S658P} is associated with a mild, non-progressive, reduction of Purkinje cells.

Cellular adaptation to the variant in the cerebellum of KI mice.

As ER stress has been implicated in the Finnish Hounds carrying *Sel1L*^{S658P} variant in the earlier study (*50*), we next asked whether and how ER homeostasis is affected in the cerebellum of *Sel1L*^{S658P} KI mice. In line with the notion that UPR sensor IRE1α is an ERAD substrate (*22*), its protein level was increased by ~4 fold. However, neither IRE1α phosphorylation nor splicing of its downstream effector *Xbp1* mRNA was significantly elevated in the cerebellum of 5-week-old KI mice (Fig. 5A). Moreover, protein levels of key ER chaperones such as BiP, GRP94, and protein disulfide isomerase (PDI) were modestly increased by ~ 30-40 and 100%, respectively, in the cerebellum of KI mice relative to those in WT littermates (Fig. 5B), in line with the notion of an adaptive cellular response to the variant. In keeping with these findings, transmission electron microscopic (TEM) examination of Purkinje cells revealed largely normal cell and ER morphologies in both 3- and 24-week-old KI mice (Fig. 5, C and D). Taken together, these data

suggest that Purkinje cells are able to adapt to the expression of *Sel1L*^{S658P} without eliciting an overt ER stress or cell death.

Purkinje cell SEL1L-HRD1 ERAD deficiency leads to progressive cerebellar ataxia.

As the aforementioned KI mice globally express the variant, we next sought to demonstrate a Purkinje cell-intrinsic role of SEL1L-HRD1 ERAD in ataxia pathogenesis. To this end, we generated a Purkinje cell-specific Sel1L-deficient mouse model (*Sel1L*^{Pcp2Cre}) by crossing *Sel1L*$^{flox/flox}$ mice (*7*) with the transgenic mice expressing Cre recombinase driven by Purkinje cell protein 2 (*Pcp2)* promoter (*54*). *Pcp2* promoter becomes active within the first postnatal week (*55*). Deletion of SEL1L in Purkinje cells reduced SEL1L and HRD1 protein levels while increasing OS9 protein levels in the cerebellum as expected (Fig. 6A and fig. S3A). Immunostaining of SEL1L confirmed the deletion of SEL1L, specifically in Purkinje cells (Fig. 6B). Unlike *Sel1L*^{S658P} mice, both male and female *Sel1L*^{Pcp2Cre} mice grew comparably to their WT *Sel1L*$^{flox/flox}$ littermates from 3 to 20 weeks of age (Fig. 6C), with normal brain weight (Fig. 6, D and E). Histological examination of the cerebellum revealed comparable Purkinje cell numbers between the two cohorts at 5 weeks of age (arrows, Fig. 6F), but significantly reduced in *Sel1L*^{Pcp2Cre} mice at 12- and 20-week of age (Fig. 6G and fig. S3B). This was further confirmed using immunostaining and Western blot analyses of calbindin (Fig. 6, H to J). Quantitation of both Purkinje cells in H&E images and Calbindin levels indeed showed a progressive loss of Purkinje cells in *Sel1L*^{Pcp2Cre} mice, starting between 5 and 12 weeks of age and reaching to a nearly 90% loss by 20 weeks of age (Fig. 6, J and K).

Since Purkinje cells represent a small fraction of cells in the cerebellum, we were unable to detect significant changes in ER stress (*Xbp1* mRNA splicing) or cell death using whole cell lysates of the cerebellum (fig. S4, A and B). Strikingly, TEM analysis revealed dilated ER and fragmented nuclei of dying Purkinje cells in the cerebellum of 9-week-old *Sel1L*^{Pcp2Cre} mice (Fig. 7A). Immunofluorescent staining revealed a moderate increase of KDEL (BiP and Grp94) expression in Purkinje cells at 5 weeks of age (Fig. 7B), in line with Western blot analyses of ER chaperons BiP and Grp94 (Fig. S4C).

At 6 weeks of age, *Sel1L*^{Pcp2Cre} mice appeared largely indistinguishable from WT littermates in gait and balance beam tests (Fig. 7, C and F, quantitated in Fig. 7, E and G, and Video S2). However, *Sel1L*^{Pcp2Cre} mice deteriorated with age and exhibited asymmetric gait and lost balance and coordination at 12 and ~20 weeks of age (Fig. 7, D and F, quantitated in Fig. 7, E and G, Video S3 and S4). Moreover, unlike *Sel1L*^{S658P} KI mice that showed abnormal hind limb-clasping reflexes at 3-9 weeks of age, *Sel1L*^{Pcp2Cre} mice started to develop hind limb-clasping reflexes around 20 weeks of age (fig. S4, D and E). Hence, these data demonstrate that, unlike *Sel1L*^{S658P} KI mice, mice with Purkinje cell-specific SEL1L-HRD1 ERAD deficiency exhibit progressive cerebellar ataxia with Purkinje cell death, starting around 9 weeks of age.

Sequence and structural analyses of *SEL1L*^{S658P}.

The aforementioned findings supported the model that *Sel1L*^{S658P} variant is hypomorphic and pathogenic in cerebellar ataxia. We next asked mechanistically how *Sel1L*^{S658P} affects ERAD function. SEL1L S658, located at the Sel1-like repeat-C (SLR-C) domain, is highly conserved from drosophila to humans, but not in yeast and plants (Fig. 8, A and B). Position-specific scoring matrix (PSSM) scores for residue 658 were positive for Ser (green) but negative for Pro (red, Fig. 8C), suggesting that Ser has been evolutionarily selected and that Pro at this position may be detrimental for SEL1L function. To visualize the structural impact of this variant, we performed the AI-based protein prediction AlphaFold analysis of the human SEL1L (1-722 aa)-HRD1 (1-334 aa)-DERLIN-OS9 protein complex (Fig. 8D). S658 resides on an α-helix close to the SEL1L amphipathic helix that directly interacts with the transmembrane 1 (TM1)–TM2 loop of HRD1 (Fig. 8, D and E).

SEL1L S658P attenuates SEL1L-HRD1 interaction.

Based on this modeling, we hypothesized that *Sel1L*^{S658P} variant may not only affect the stability of SEL1L (by destabilizing the helix), but also interfere with the formation of the ERAD complex, consisting of DERLIN, UBE2J1, OS9, and ERLEC1 (Fig. 9A) (*56*). In *SEL1L*$^{-/-}$ HEK293T cells transfected with FLAG-tagged SEL1L (WT or S658P), *Sel1L*^{S658P} markedly attenuated the interaction between SEL1L and endogenous HRD1 compared to WT SEL1L, while having no effect on its interaction with other components of the complex including OS9, ERLEC1, UBE2J1, and DER2 (Fig. 9, B and C). Furthermore, mutation of Ser at this position to

Ala (S658A) had no effect on SEL1L-HRD1 interaction (lane 4, fig. S5A), while S658D or K attenuated the interaction, albeit not as dramatically as S658P (lane 5-6 vs. 3, fig. S5A). Indeed, both D and K at this position have negative PSSM scores while A has a positive score (Fig. 8C). None of these mutations at S658 SEL1L affected its interaction with OS9 or UBE2J1 (fig. S5A). Mutating P658 back to S (P658S) rescued the interaction between SEL1L and HRD1 (lane 7, fig. S5A), excluding the possibility of additional off-target mutations responsible for the disruption caused by *Sel1L*^{S658P}. Mutation of a nearby Ser at position 663, 5 amino acids downstream of S658 located at the loop between the two α-helices (fig. S5B), to Pro (S663P) had no apparent effect on the formation of SEL1L-HRD1 complex (lane 8, fig. S5A). In line with the overexpression experiments, SEL1L interaction with HRD1 was reduced by 5-fold in KI livers, while having no effect on the interactions with OS9 and ERLEC1, compared to WT and HET livers (Fig. 9D). Hence, *Sel1L*^{S658P} attenuates the interaction between SEL1L and HRD1, i.e. disrupting the formation of the SEL1L-HRD1 complex.

SEL1L^{S658P} is a hypomorphic variant.

We next asked whether *Sel1L*^{S658P} is a hypomorphic variant. We first tested the turnover and aggregation of a known ERAD substrate, a disease mutant of pro-arginine vasopressin (proAVP) at residue 57 (Gly-to-Ser, Gly57Ser) (*25, 27*). In line with our previous studies (*25, 27*), proAVP Gly57Ser protein accumulated and formed HMW aggregates in *SEL1L*$^{-/-}$ HEK293T cells (Fig. 9E, lane 2 vs. 1), which was attenuated upon the over-expression of SEL1L WT (lane 3-5 vs. 2), but not SEL1L S658P (lane 6-8 vs. 3-5, Fig. 9E and quantitated in fig. S5C).

We then generated KI HEK293T cells carrying the bi-allelic variant (fig. S6, A and B) and compared them to WT and *SEL1L*$^{-/-}$ HEK293T cells. Both KI and KO cell lines were generated using the CRISPR/Cas9 system. Protein levels of SEL1L and HRD1 were reduced by 25 and 60%, respectively, in *SEL1L*^{S658P} KI HEK293T cells compared to WT HEK293T cells (Fig. 9, F and G), in keeping with the notion that the SEL1L-HRD1 interaction is required for its stability (*7*). However, the reduction in HRD1 protein was modest compared to that in *SEL1L*$^{-/-}$ HEK293T cells (Fig. 9, F and G). Moreover, *SEL1L*^{S658P} expression led to a mild, but significant, accumulation of several known ERAD substrates such as IRE1α, OS9, and CD147 in KI cells compared to those in WT HEK293T cells, but to a much less extent compared to those in *SEL1L*$^{-}$

$^{/-}$ HEK293T cells (Fig. 9, F and G). Hence, these data demonstrate that *SEL1L*^{S658P} is a hypomorphic variant with partial ERAD dysfunction.

Identification of ASTROTACTIN 1/2 (ASTN1/2) as endogenous ERAD substrates.

Our forementioned data supported the model that ERAD variants may cause disease in a substrate-specific manner, independently of ER stress or apoptosis. To further explore this possibility, we performed proteomics screen of the SEL1L interactome to identify ERAD substrates in neuroblastoma N2a cells with or without SEL1L or HRD1 (Fig. 10A). This experimental design was based on the assumption that the interactions between SEL1L and substrates are prolonged in the absence of HRD1 as demonstrated by the strong interaction between SEL1L and proAVP(G57S) in *HRD1*$^{-/-}$ cells, but not *WT* HEK293T cells (fig. S7A). Upon stringent cut-off criteria placed on the IP-MS data to select for proteins detected only in *HRD1*$^{-/-}$ cells, we identified a total of 17 hits (Fig. 10B and fig. S7B). Excitingly, one of the top candidates was ASTN1, a double-span transmembrane protein with the glycosylation sites and 17 intramolecular disulfide bonds (fig. S7C), involved in neuronal migration and synaptic plasticity. Mice lacking ASTN1 are also smaller and have poorer balance and coordination (*57*). Indeed, both ASTN1 and its homolog ASTN2 are enriched in the brain (*58*) (fig. S7, C and D) and are cleaved at the second transmembrane domain and the resulting two fragments are connected with a disulfide bond (*59*) (fig. S7C).

We next tested whether ASTN1 and 2 are endogenous SEL1L-HRD1 ERAD substrates. The interaction between endogenous or transfected ASTN1 and endogenous SEL1L was confirmed using immunoprecipitation followed by western blot (Fig. 10C and fig. S7E). ASTN1 protein was ubiquitinated and degraded in an HRD1- and proteasomal-dependent manner (Fig. 10D). Indeed, in ASTN1/2 protein levels were increased by 10 folds in cells lacking SEL1L or HRD1 (Fig. 10E), while mRNA levels of *Astn1/2* were unchanged (fig. S7F). ASTN1/2 proteins were highly unstable in WT N2a cells with a half-life less than 2-4 hr, but were largely stabilized in the absence of ERAD (Fig. 10F and fig. S7G). Similarly, basal levels of ASTN1/2 proteins were doubled in the cerebellum of KI mice (Fig. 10G), uncoupled from the gene transcription (fig. S7H). Endo H (E) and PNGase F (P) digestion revealed that nearly half of ASTN2 was EndoH-sensitive in the cerebellum of KI mice vs. 5% in WT littermates (Fig. 10H), indicative of

increased ER retention in cells with SEL1L-HRD1 ERAD dysfunction. Further non-reducing SDS-PAGE followed by Western blot showed increased HMW aggregates of ASTN proteins, formed via intermolecular disulfide bonds, in the cerebellum of KI mice (Fig. 10I). Hence, ASTN1/2 proteins are bona fide substrates of SEL1L-HRD1 ERAD, with elevated ER retention and aggregation when ERAD function is impaired.

DISCUSSION

Both the role of SEL1L-HRD1 ERAD in the pathogenesis of cerebellar ataxia and the nature of cerebellar ataxia-causing genes remain an enigma. Here we provide definitive evidence supporting the model showing that defects in SEL1L-HRD1 protein complex formation and function drive cerebellar ataxia in mice. This is demonstrated in two mouse models, Purkinje cell-specific SEL1L KO mice and global KI mice expressing *SEL1L*^{S658P} variant, previously identified in Finnish Hounds with cerebellar ataxia *(50)*. The development of ataxia is progressive in the Purkinje cell-specific SEL1L KO mouse model and associated with a progressive loss of Purkinje cells via apoptosis, which is characteristic of cerebellar ataxia (*60*). While our data show that *SEL1L*^{S658P} variant is indeed pathogenic, it causes early onset, non-progressive, mild cerebellar ataxia in mice. Indeed, unlike the KO mouse model, *SEL1L*^{S658P} variant does not cause a progressive increase of Purkinje cell death, as we found no evidence of apoptosis. Rather, we speculate that it may affect Purkinje cell development or differentiation as we recently described for pancreatic β cells (*29*). Mechanistically, we further show that *SEL1L*^{S658P} variant impairs ERAD function by attenuating SEL1L-HRD1 interaction. Hence, this study demonstrate that the SEL1L-HRD1 complex and its function in Purkinje cells play an essential role in cerebellar ataxia pathogenesis.

Purkinje cells are some of the largest neurons in the brain with a prominent ER structure that form an interconnected network regulating calcium signaling, protein synthesis, folding, and protein trafficking (*61*). Previous studies have shown that Purkinje cells are vulnerable to alterations in ER homeostasis, as they have a high demand for protein synthesis to maintain a

large number of synapsis (*62, 63*). Our data show that Purkinje cells are able to adapt to hypomorphic, but not to a complete loss of, SEL1L-HRD1 ERAD function. The effect of SEL1L-HRD1 ERAD in Purkinje cells may be through both ER stress-dependent and -independent manners. In keeping with ER stress-independent mechanism, we observed no obvious ER dilation or an overt UPR activation in Purkinje cells of the KI mice. The lack of UPR induction in the KI model is likely due to various adaptive mechanisms in response to the hypomorphic variant, including, but not limited to, the upregulation of ER chaperones to increase folding efficiency and enhanced aggregation and sequestration of misfolded proteins to hence attenuate proteotoxicity. Our proteomic screen followed by biochemical studies identified both ASTN1 and ASTN2 proteins as ERAD substrates. Both proteins are quickly degraded by SEL1L-HRD1 ERAD and accumulated in the ER of ERAD-deficient cells. Indeed, defects in the function of ASTN proteins in humans have been linked to neurodevelopmental symptoms such as developmental delay, intellectual disability and cerebellar dysfunction (*58, 64-66*). Hence, we propose that impaired function of specific SEL1L-HRD1 ERAD substrate(s) such as ASTN1/2 may underlie, at least in part, cerebellar ataxia of our KI mice. On the other hand, *SEL1L* KO Purkinje cells may undergo cell death due to the accumulation of misfolded proteins in the ER, which may lead to insurmountable stress in the ER for Purkinje cells with age. Future studies are required to further identify additional SEL1L-HRD1 ERAD substrates and delineate their importance in Purkinje cell development and function.

This study reveals the pathogenic nature of $SEL1L^{S658P}$ variant and its underlying mechanism in mammals in the pathogenesis of cerebellar ataxia. $SEL1L^{S658P}$ resides in close proximity to the interface between SEL1L and HRD1, thereby disrupting the interaction between SEL1L and its E3 ligase HRD1. These unexpected findings not only change our current view on the pathological importance of SEL1L- HRD1 ERAD and its interaction in mammals, but also provide an important target and framework for future therapeutic design targeting SEL1L-HRD1 ERAD function using small molecules.

AUTHOR CONTRIBUTIONS

L.L.L. and M.T. collaboratively designed and performed most experiments; X.W. performed the structural analysis; B.P., Z.J.L., H.H.L., H.M., H.W. and Y.L. assisted with some *in vitro* and *in vivo* experiments; X.L. and Z.Z. performed MRI and involved in experimental design; Z.Z. and S.S. provided insightful discussion; M.H., E.E.G., and M.E.H. generated ASTN1/2 antibodies; S.S. and L.Q. directed the study and wrote the manuscript with help from L.L.L and M.T.; L.L.L. and M.T. wrote the methods and figure legends; all authors commented on and approved the manuscript.

ACKNOWLEDGEMENTS

We acknowledge Qing Zhu, Xiang Gao, David Olson and the Molecular Genetics Core of the Michigan Diabetes Research Center for the design and screening of the knock-in mice founder animals; Thomas L. Saunders, Elizabeth Hughes, Wanda Filipiak, Galina Gavrilina, Honglai Zhang and the Transgenic Animal Model Core of the University of Michigan's Biomedical Research Core Facilities for transgenic animal production. We thank Drs. Ingrid Bergin and Kendra Andrie (the ULAM In-Vivo Animal Core at University of Michigan Medical School) for the pathological analyses; Chih-Chi Andrew Hu (Houston Methodist Hospital) for reagents; members of the Qi and Arvan laboratories at the University of Michigan Medical School for technical assistance and insightful discussions; and animal phenotyping cores (NIH P30AR069620, P30DK020572, P30DK089503 and 1U2CDK110678-01), and the ULAM In-Vivo Animal Core at University of Michigan Medical School for sample processing and blind behavioral studies. This work was supported by RF1NS122060 (Z.Z.), R01DK128077, R01DK132068 (S.S.), R01DK120047, R01DK120330, R35GM130292 and Michigan Protein Folding Disease Initiative (L.Q.). L.L.L. and Z.J.L. are supported in part by National Ataxia Foundation Post- and Pre-doctoral Fellowships (NAF 918037 and 1036307). S.S. and L.Q. would like to delicate this paper to the loving memories of Nian-Nian Sun Qi (2/7/23) and Dian-Dian Sun Qi (4/4/22).

Competing interests: The authors declare no conflict of interest.

Data and materials availability: The materials and reagents used are either commercially available or available upon the request. Proteomics data has been deposited into a public database PRIDE (PXD035114). All other data are available in the main text or Supplemental Materials.

REFERENCES

1. J. A. Olzmann, R. R. Kopito, J. C. Christianson, The Mammalian Endoplasmic Reticulum-Associated Degradation System. *Cold Spring Harbor perspectives in biology* **5**, (2013).
2. J. Hwang, L. Qi, Quality Control in the Endoplasmic Reticulum: Crosstalk between ERAD and UPR pathways. *Trends Biochem Sci* **43**, 593-605 (2018).
3. L. Qi, B. Tsai, P. Arvan, New Insights into the Physiological Role of Endoplasmic Reticulum-Associated Degradation. *Trends Cell Biol* **27**, 430-440 (2017).
4. R. Y. Hampton, R. G. Gardner, J. Rine, Role of 26S proteasome and HRD genes in the degradation of 3-hydroxy-3-methylglutaryl-CoA reductase, an integral endoplasmic reticulum membrane protein. *Mol Biol Cell* **7**, 2029-2044 (1996).
5. J. Bordallo, R. K. Plemper, A. Finger, D. H. Wolf, Der3p/Hrd1p is required for endoplasmic reticulum-associated degradation of misfolded lumenal and integral membrane proteins. *Mol Biol Cell* **9**, 209-222 (1998).
6. M. Kikkert *et al.*, Human HRD1 is an E3 ubiquitin ligase involved in degradation of proteins from the endoplasmic reticulum. *J Biol Chem* **279**, 3525-3534 (2004).
7. S. Sun *et al.*, Sel1L is indispensable for mammalian endoplasmic reticulum-associated degradation, endoplasmic reticulum homeostasis, and survival. *Proc Natl Acad Sci U S A* **111**, E582-591 (2014).
8. R. G. Gardner *et al.*, Endoplasmic reticulum degradation requires lumen to cytosol signaling. Transmembrane control of Hrd1p by Hrd3p. *J Cell Biol* **151**, 69-82 (2000).
9. R. Gauss, T. Sommer, E. Jarosch, The Hrd1p ligase complex forms a linchpin between ER-lumenal substrate selection and Cdc48p recruitment. *EMBO J* **25**, 1827-1835 (2006).
10. M. Mehnert *et al.*, The interplay of Hrd3 and the molecular chaperone system ensures efficient degradation of malfolded secretory proteins. *Mol Biol Cell* **26**, 185-194 (2015).
11. B. Mueller, B. N. Lilley, H. L. Ploegh, SEL1L, the homologue of yeast Hrd3p, is involved in protein dislocation from the mammalian ER. *J Cell Biol* **175**, 261-270 (2006).
12. J. C. Christianson, T. A. Shaler, R. E. Tyler, R. R. Kopito, OS-9 and GRP94 deliver mutant alpha1-antitrypsin to the Hrd1-SEL1L ubiquitin ligase complex for ERAD. *Nat Cell Biol* **10**, 272-282 (2008).
13. B. Mueller, E. J. Klemm, E. Spooner, J. H. Claessen, H. L. Ploegh, SEL1L nucleates a protein complex required for dislocation of misfolded glycoproteins. *Proc Natl Acad Sci USA* **105**, 12325-12330 (2008).
14. N. Hosokawa *et al.*, Human XTP3-B forms an endoplasmic reticulum quality control scaffold with the HRD1-SEL1L ubiquitin ligase complex and BiP. *J Biol Chem* **283**, 20914-20924 (2008).
15. P. Carvalho, V. Goder, T. A. Rapoport, Distinct ubiquitin-ligase complexes define convergent pathways for the degradation of ER proteins. *Cell* **126**, 361-373 (2006).
16. N. Vashistha, S. E. Neal, A. Singh, S. M. Carroll, R. Y. Hampton, Direct and essential function for Hrd3 in ER-associated degradation. *Proc Natl Acad Sci U S A* **113**, 5934-5939 (2016).
17. A. B. Francisco *et al.*, Deficiency of suppressor enhancer lin12 1 like (SEL1L) in mice leads to systemic endoplasmic reticulum stress and embryonic lethality. *J Biol Chem* **285**, 13694-13703 (2010).
18. N. Yagishita *et al.*, Essential role of synoviolin in embryogenesis. *J Biol Chem* **280**, 7909-7916 (2005).
19. H. Fujita *et al.*, The E3 ligase synoviolin controls body weight and mitochondrial biogenesis through negative regulation of PGC-1beta. *EMBO J* **34**, 1042-1055 (2015).
20. A. Bhattacharya, L. Qi, ER-associated degradation in health and disease - from substrate to organism. *J Cell Sci* **132**, jcs232850 (2019).
21. H. Sha *et al.*, The ER-associated degradation adaptor protein Sel1L regulates LPL secretion and lipid metabolism. *Cell Metab* **20**, 458-470 (2014).

22. S. Sun *et al.*, IRE1a is an endogenous substrate of endoplasmic-reticulum-associated degradation. *Nat Cell Biol* **17**, 1546-1555 (2015).
23. Y. Ji *et al.*, The Sel1L-Hrd1 Endoplasmic Reticulum-Associated Degradation Complex Manages a Key Checkpoint in B Cell Development. *Cell reports* **16**, 2630-2640 (2016).
24. S. Sun *et al.*, Epithelial Sel1L is required for the maintenance of intestinal homeostasis. *Mol Biol Cell* **27**, 483-490 (2016).
25. G. Shi *et al.*, ER-associated degradation is required for vasopressin prohormone processing and systemic water homeostasis. *J Clin Invest* **127**, 3897-3912 (2017).
26. A. Bhattacharya *et al.*, Hepatic Sel1L-Hrd1 ER-associated degradation (ERAD) manages FGF21 levels and systemic metabolism via CREBH. *EMBO J* **37**, e99277 (2018).
27. G. H. Kim *et al.*, Hypothalamic ER-associated degradation regulates POMC maturation, feeding and age-associated obesity. *J Clin Invest* **128**, 1125-1140 (2018).
28. L. Liu *et al.*, ER-associated degradation preserves hematopoietic stem cell quiescence and self-renewal by restricting mTOR activity. *Blood* **136**, 2975-2986 (2020).
29. N. Shrestha *et al.*, Sel1L-Hrd1 ER-associated degradation maintains β cell identity via TGFβ signaling. *J Clin Invest* **130**, 3499-3510 (2020).
30. N. Shrestha, R. B. Reinert, L. Qi, Endoplasmic Reticulum Protein Quality Control in beta Cells. *Semin Cell Dev Biol* **103**, 59-67 (2020).
31. T. Wu *et al.*, HRD1 an important player in pancreatic beta-cell failure and therapeutic target for type 2 diabetic mice. *Diabetes*, (2020).
32. L. Xu *et al.*, Protein quality control through endoplasmic reticulum-associated degradation maintains haematopoietic stem cell identity and niche interactions. *Nat Cell Biol* **22**, 1162-1169 (2020).
33. Z. Zhou *et al.*, Endoplasmic reticulum-associated degradation regulates mitochondrial dynamics in brown adipocytes. *Science* **368**, 54-60 (2020).
34. X. Liu *et al.*, Notch-induced endoplasmic reticulum-associated degradation governs mouse thymocyte beta- selection. *eLife* **10**, (2021).
35. S. Yoshida *et al.*, Endoplasmic reticulum-associated degradation is required for nephrin maturation and kidney glomerular filtration function. *J Clin Invest* **131**, (2021).
36. T. Wu *et al.*, Hrd1 suppresses Nrf2-mediated cellular protection during liver cirrhosis. *Genes Dev* **28**, 708-722 (2014).
37. H. Yang *et al.*, Hrd1-mediated BLIMP-1 ubiquitination promotes dendritic cell MHCII expression for CD4 T cell priming during inflammation. *J Exp Med* **211**, 2467-2479 (2014).
38. S. Kong *et al.*, Endoplasmic reticulum-resident E3 ubiquitin ligase Hrd1 controls B-cell immunity through degradation of the death receptor CD95/Fas. *Proc Natl Acad Sci U S A* **113**, 10394-10399 (2016).
39. Y. Xu *et al.*, The ER membrane-anchored ubiquitin ligase Hrd1 is a positive regulator of T-cell immunity. *Nature communications* **7**, 12073 (2016).
40. J. Wei *et al.*, HRD1-ERAD controls production of the hepatokine FGF21 through CREBH polyubiquitination. *EMBO J* **37**, e98942 (2018).
41. G. Shi *et al.*, ER-associated degradation is required for vasopressin prohormone processing and systemic water homeostasis. *J Clin Invest* **127**, 3897-3912 (2017).
42. G. H. Kim *et al.*, Hypothalamic ER-associated degradation regulates POMC maturation, feeding, and age-associated obesity. *J Clin Invest* **128**, 1125-1140 (2018).
43. F. Taroni, S. DiDonato, Pathways to motor incoordination: the inherited ataxias. *Nat Rev Neurosci* **5**, 641-655 (2004).
44. S. Jayadev, T. D. Bird, Hereditary ataxias: overview. *Genet Med* **15**, 673-683 (2013).
45. J. Beckinghausen, R. V. Sillitoe, Insights into cerebellar development and connectivity. *Neurosci Lett* **688**, 2-13 (2019).
46. A. H. Koeppen, The neuropathology of the adult cerebellum. *Handb Clin Neurol* **154**, 129-149 (2018).

47. J. Gandhi *et al.*, Protein misfolding and aggregation in neurodegenerative diseases: a review of pathogeneses, novel detection strategies, and potential therapeutics. *Rev Neurosci* **30**, 339-358 (2019).
48. J. L. Zambonin *et al.*, Spinocerebellar ataxia type 29 due to mutations in ITPR1: a case series and review of this emerging congenital ataxia. *Orphanet J Rare Dis* **12**, 121 (2017).
49. H. Ando, M. Hirose, K. Mikoshiba, Aberrant IP(3) receptor activities revealed by comprehensive analysis of pathological mutations causing spinocerebellar ataxia 29. *Proc Natl Acad Sci U S A* **115**, 12259-12264 (2018).
50. K. Kyostila *et al.*, A SEL1L mutation links a canine progressive early-onset cerebellar ataxia to the endoplasmic reticulum-associated protein degradation (ERAD) machinery. *PLoS Genet* **8**, e1002759 (2012).
51. E. Tara, A. Vitenzon, E. Hess, K. Khodakhah, Aberrant cerebellar Purkinje cell activity as the cause of motor attacks in a mouse model of episodic ataxia type 2. *Dis Model Mech* **11**, (2018).
52. P. A. Egorova, O. A. Zakharova, O. L. Vlasova, I. B. Bezprozvanny, In vivo analysis of cerebellar Purkinje cell activity in SCA2 transgenic mouse model. *J Neurophysiol* **115**, 2840-2851 (2016).
53. J. T. Walter, K. Alvina, M. D. Womack, C. Chevez, K. Khodakhah, Decreases in the precision of Purkinje cell pacemaking cause cerebellar dysfunction and ataxia. *Nat Neurosci* **9**, 389-397 (2006).
54. J. J. Barski, K. Dethleffsen, M. Meyer, Cre recombinase expression in cerebellar Purkinje cells. *Genesis* **28**, 93-98 (2000).
55. A. Slugocka, J. Wiaderkiewicz, J. J. Barski, Genetic Targeting in Cerebellar Purkinje Cells: an Update. *Cerebellum* **16**, 191-202 (2017).
56. J. Schulz *et al.*, Conserved cytoplasmic domains promote Hrd1 ubiquitin ligase complex formation for ER-associated degradation (ERAD). *J Cell Sci* **130**, 3322-3335 (2017).
57. N. C. Adams, T. Tomoda, M. Cooper, G. Dietz, M. E. Hatten, Mice that lack astrotactin have slowed neuronal migration. *Development* **129**, 965-972 (2002).
58. A. C. Lionel *et al.*, Disruption of the ASTN2/TRIM32 locus at 9q33.1 is a risk factor in males for autism spectrum disorders, ADHD and other neurodevelopmental phenotypes. *Hum Mol Genet* **23**, 2752-2768 (2014).
59. P. Lara *et al.*, Murine astrotactins 1 and 2 have a similar membrane topology and mature via endoproteolytic cleavage catalyzed by a signal peptidase. *J Biol Chem* **294**, 4538-4545 (2019).
60. M. Girard *et al.*, Mitochondrial dysfunction and Purkinje cell loss in autosomal recessive spastic ataxia of Charlevoix-Saguenay (ARSACS). *Proc Natl Acad Sci U S A* **109**, 1661-1666 (2012).
61. A. Villa *et al.*, The endoplasmic reticulum of Purkinje neuron body and dendrites: molecular identity and specializations for Ca2+ transport. *Neuroscience* **49**, 467-477 (1992).
62. L. Zhao, C. Rosales, K. Seburn, D. Ron, S. L. Ackerman, Alteration of the unfolded protein response modifies neurodegeneration in a mouse model of Marinesco-Sjogren syndrome. *Hum Mol Genet* **19**, 25-35 (2010).
63. Y. Yang *et al.*, Disruption of Tmem30a results in cerebellar ataxia and degeneration of Purkinje cells. *Cell death & disease* **9**, 899 (2018).
64. W. Wiszniewski *et al.*, Comprehensive genomic analysis of patients with disorders of cerebral cortical development. *Eur J Hum Genet* **26**, 1121-1131 (2018).
65. S. Anazi *et al.*, Clinical genomics expands the morbid genome of intellectual disability and offers a high diagnostic yield. *Mol Psychiatry* **22**, 615-624 (2017).
66. S. Maddirevula *et al.*, Exploiting the Autozygome to Support Previously Published Mendelian Gene-Disease Associations: An Update. *Front Genet* **11**, 580484 (2020).

FIGURE LEGENDS

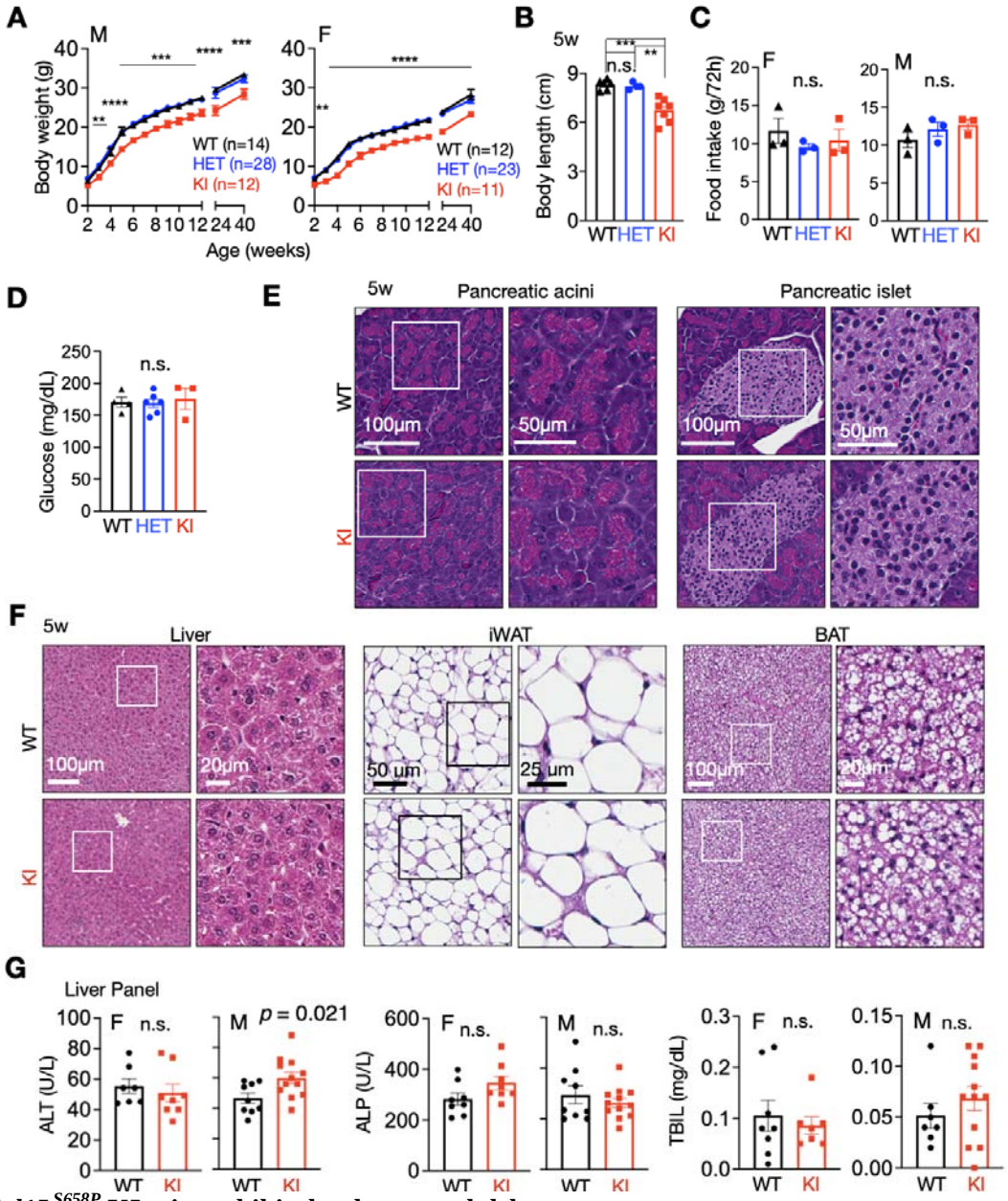

Fig. 1. *Sel1L*^{S658P} KI mice exhibit developmental delay.
(A) Growth curve. n = 11-28 mice for male and n = 11-23 mice for female per group. **(B)** Body length of 5-week-old mice of both genders (n = 4-7 mice per group). **(C)** 72 hr food intake of 5-week-old mice of both genders (n = 3 mice per group). n.s. is comparing all the groups. **(D)** Ad libitum blood glucose levels of 5-week-old mice (n = 3-6 mice per group). n.s. is comparing all the groups. **(E-F)** Hematoxylin & eosin (H&E) images of various peripheral tissues (**E**, pancreatic acini and islet; **F**, Liver, iWAT and BAT) from 5-week-old mice (n = 3 mice per group). iWAT, inguinal white adipose tissue; BAT, brown adipose tissue. **(G)** Serum levels of alanine transaminase (ALT), total bilirubin (TBIL) and alkaline phosphatase (ALP) in 5-week-old mice of both sexes (n = 7-12 mice per group). Data are presented as mean ± SEM. n.s., not significant; **p<0.01, ***p<0.001 and ****p<0.0001 by two-way ANOVA followed by Tukey's multiple comparisons test for each age (A), one-way ANOVA followed by Tukey's post hoc test (B) and two-tailed Student's *t*-test (G).

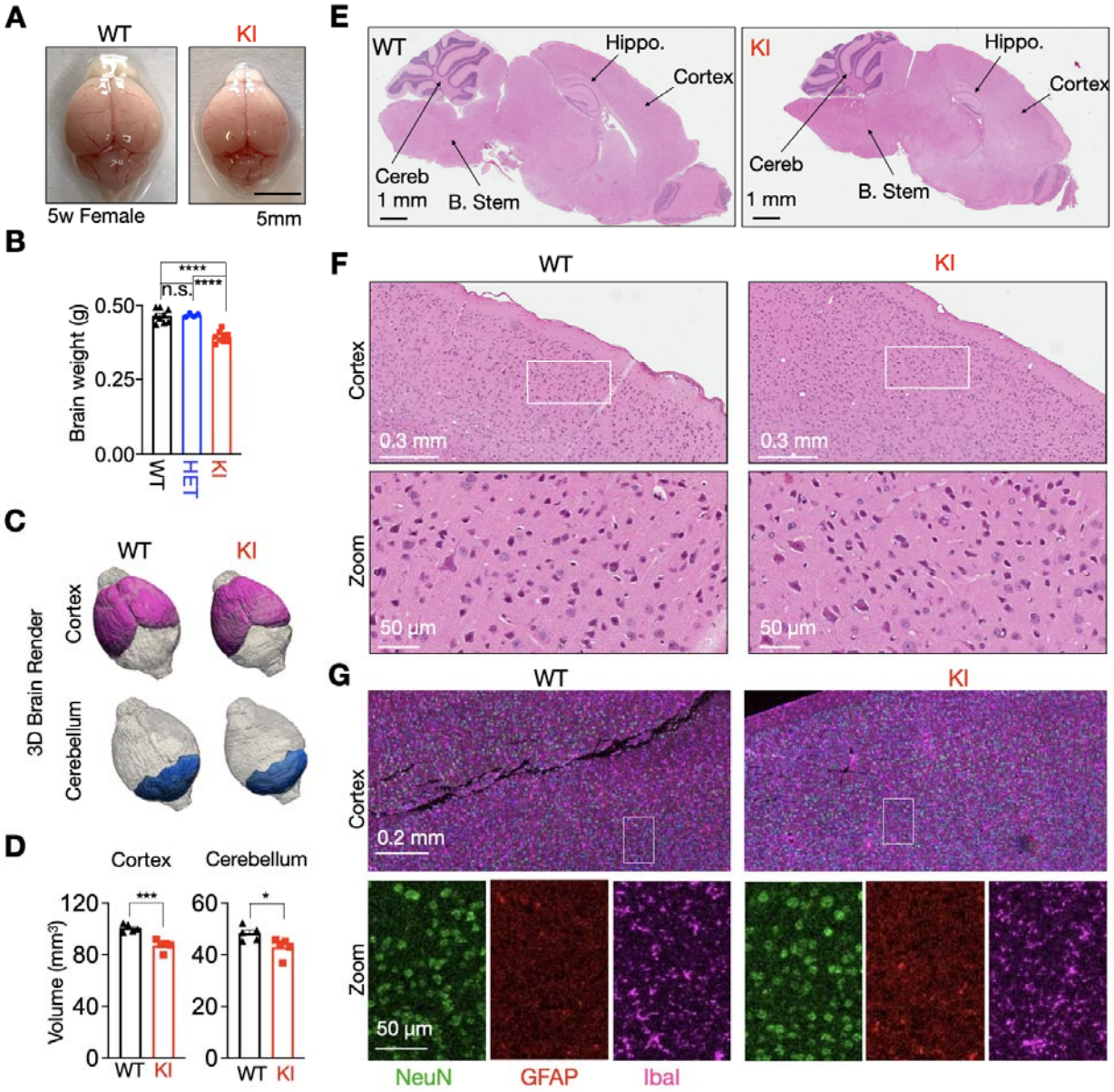

Fig. 2. *Sel1L*^{S658P} KI mice exhibit microcephaly.
(A-B) Representative pictures of brains from 5-week-old mice, with quantitation of brain weight shown in (**B**) (n = 9, 4 and 9 mice for WT, HET and KI). **(C-D)** 3D rendering of cortex and cerebellum from 5-week-old mice, with quantitation shown in (**D**) (n = 5 mice per group). **(E-F)** Hematoxylin & eosin (H&E) stained sagittal sections of whole brain (**E**) and cortex (**F**) from 5-week-old mice (n = 3 mice per group). Hippo., hippocampus; B. Stem, brain stem; Cereb., cerebellum. **(G)** Representative confocal images of NeuN (green), GFAP (red) and Iba1 (purple) for neurons, astrocytes and microglia in the brains of 5-week-old mice (n = 2 mice per group). Staining of the whole brain is shown in (Fig. S2B). "Data are presented as mean ± SEM. n.s., not significant; *p<0.05, ***p<0.001 and ****p<0.0001 by one-way ANOVA followed by Tukey's post hoc test (B) and two-tailed Student's *t*-test (D).

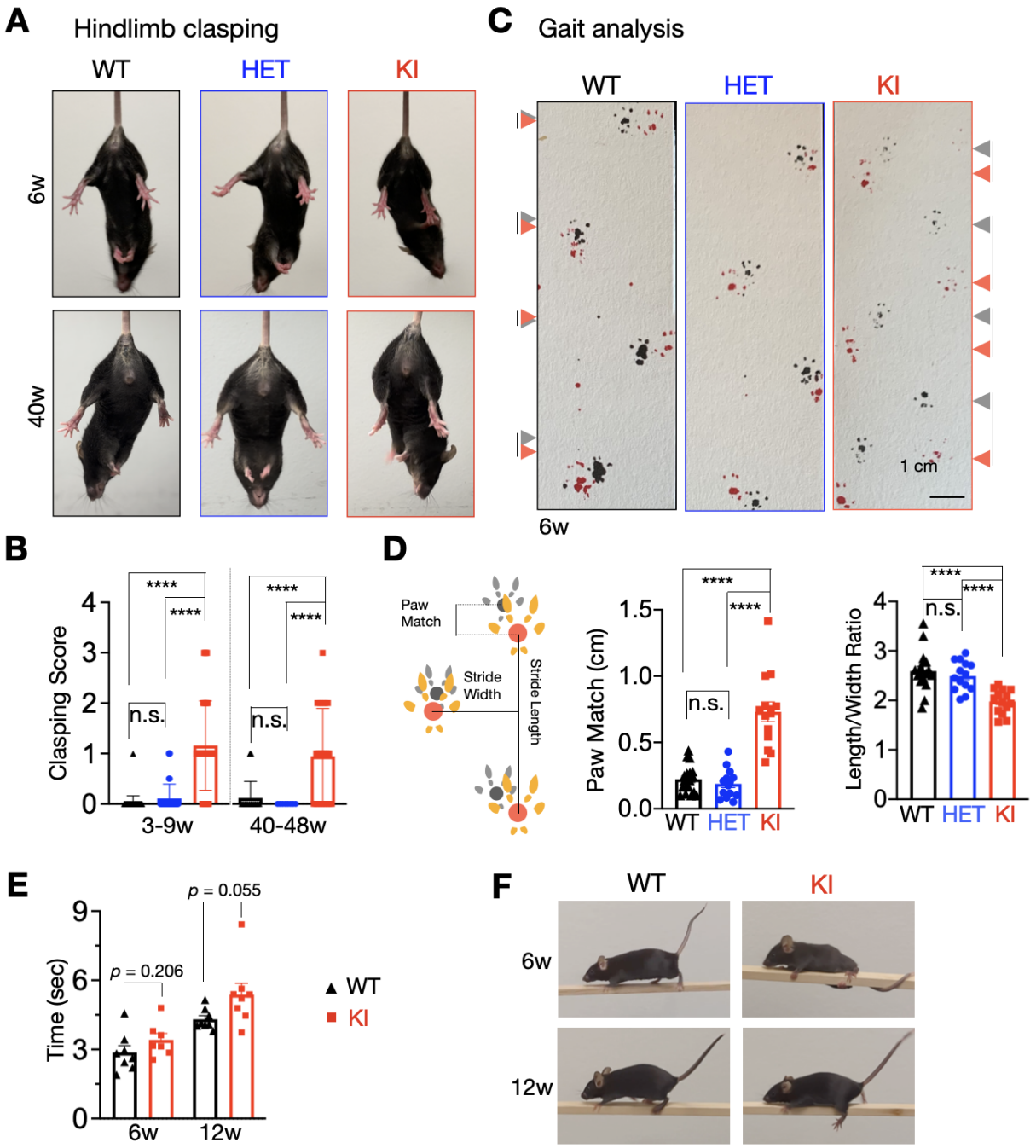

Fig. 3. *Sel1L*^{S658P} KI mice exhibit early-onset, non-progressive, mild ataxia.
(A-B) Representative pictures of hindlimb clasping (**A**) and score quantitation (**B**) of 3-9 (n = 49, 51 and 38 for WT, HET and KI) and 40-48 (n = 17, 8 and 20 mice for WT, HET and KI) -week-old littermates of both genders. **(C-D)** Representative pictures (**C**), cartoon schematic of paw prints (left, **D**) and quantitation of gait analysis (right, **D**) of 6-week-old littermates of both genders. The grey and red arrows in (**C**) indicate forelimb and hindlimb, respectively; and the lines between grey and red arrow indicate the distance between the two limbs (n = 14-18 mice per group). **(E)** Quantification of balance beam test from mice at 6 and 12 weeks of age (n = 7-8 per group). **(F)** Representative pictures of slips of 6 and 12-week-old KI mice on balance beam. **(G)** Data are presented as mean ± SEM. n.s., not significant. ****p<0.0001 by one-way ANOVA followed by Tukey's post hoc test (B, D) and two-tailed Student's *t*-test (E).

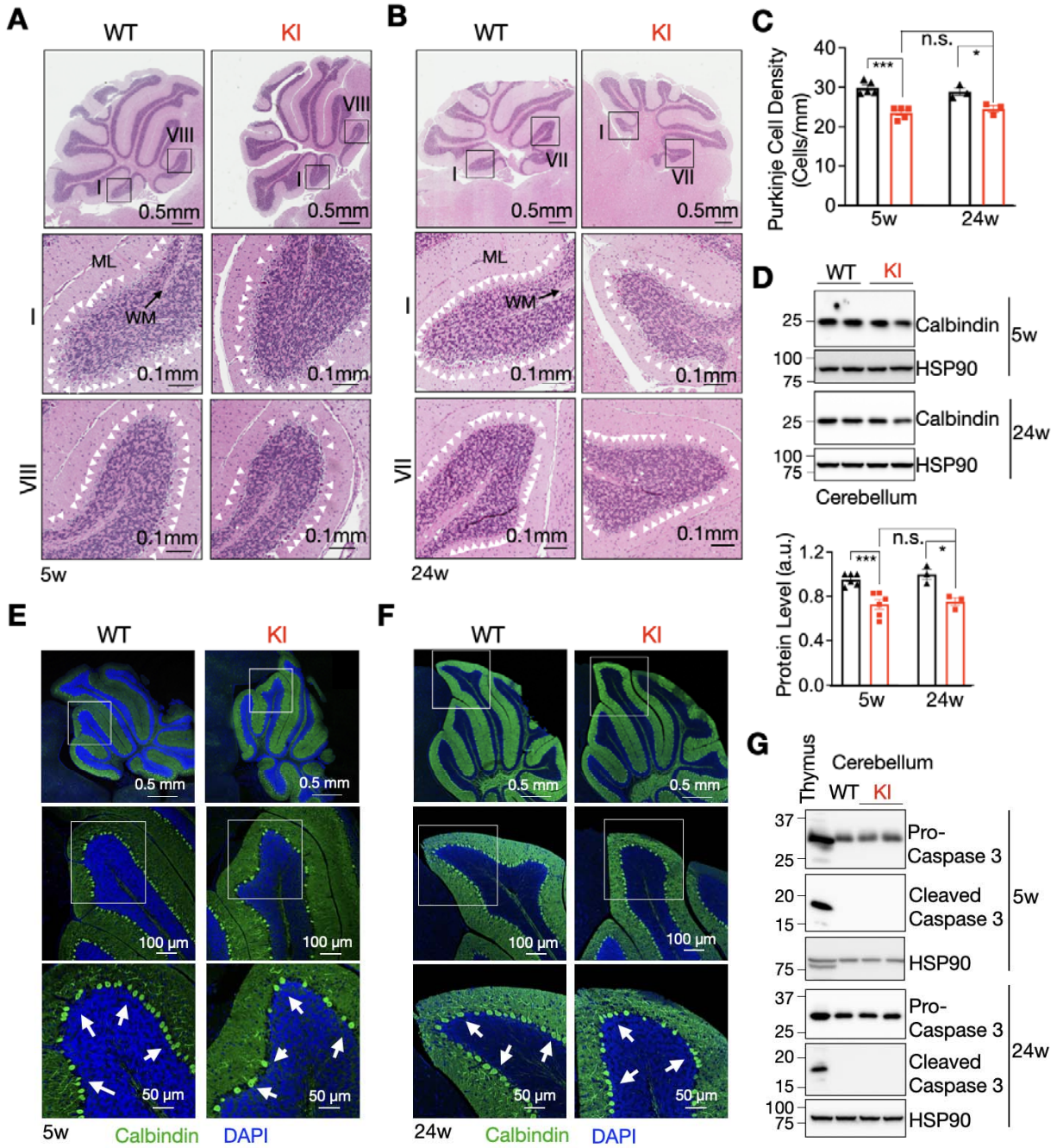

Fig. 4. *Sel1L*^{S658P} KI mice exhibit an early onset, non-progressive, mild reduction of Purkinje cells. **(A-C)** Hematoxylin & eosin (H&E) stained sagittal sections of the cerebellum from 5- (**A**) and 24- (**B**) week-old mice, with quantitation of Purkinje cell density shown in (**C**) (n = 3-5 mice per group). White arrowheads, Purkinje cells. ML, molecular layer; MW, white matter. **(D)** Western blot analysis of cerebellum of 5- and 24-week-old mice with quantitation shown below (n = 3-6 mice per group). **(E-F)** Representative confocal images of Calbindin (green) in the cerebellum of 5- (**E**) and 24- (**F**) week-old mice. White arrows, Purkinje cells (n = 3 mice per group). **(G)** Western blot analysis of cell death in the cerebellum of 5- and 24-week-old mice. The thymus, a positive control (n = 2 mice per group). Data are presented as mean ± SEM. n.s., not significant. *p<0.05 and ***p<0.001 by two-tailed Student's *t*-test (C, D).

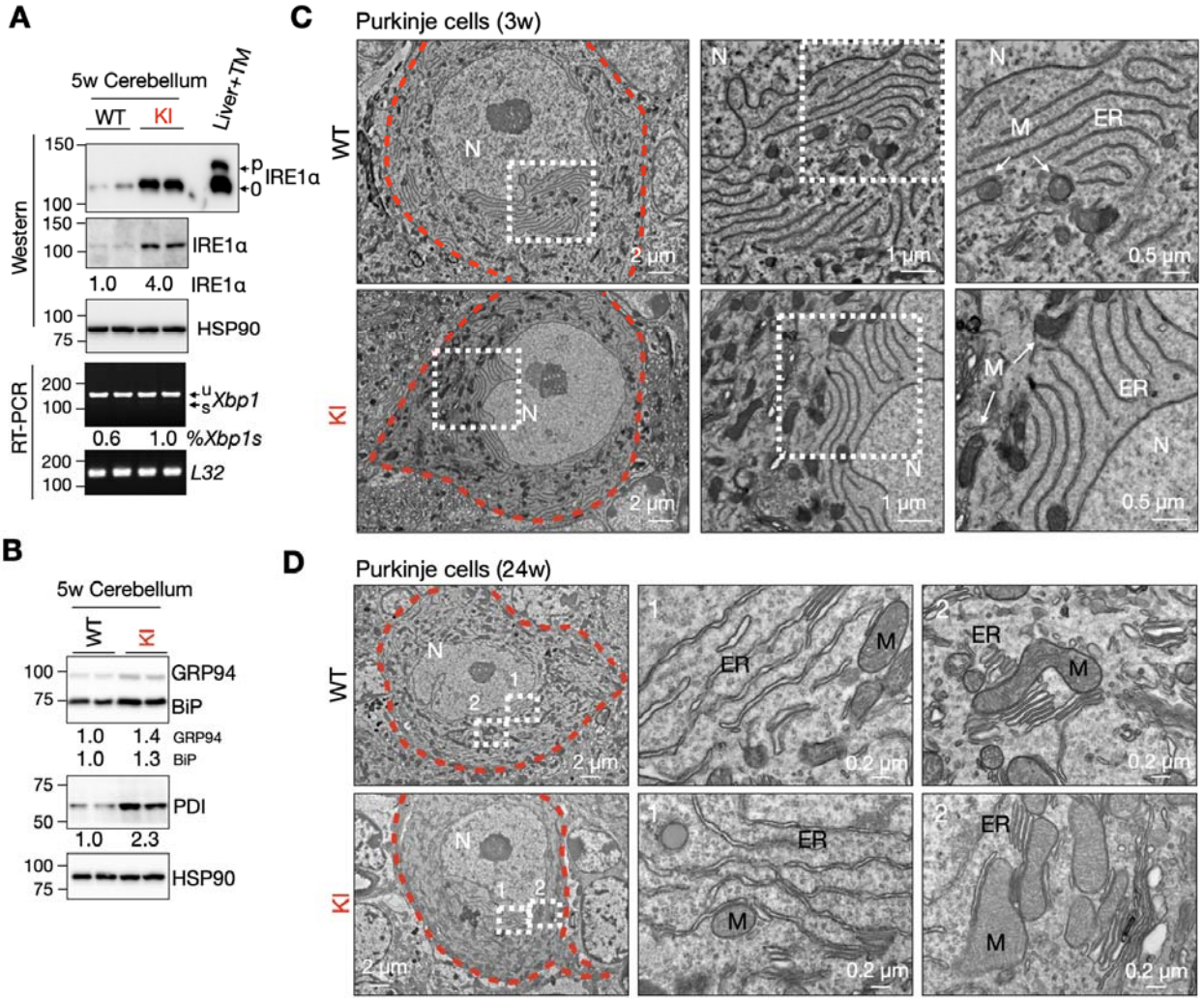

Fig. 5. Subtle alteration of ER homeostasis in the cerebellum of *Sel1L*^{S658P} KI mice.
(A) Western blot analysis of IRE1α phosphorylation (top) and RT-PCR of *Xbp1* splicing in the cerebellum of 5-week-old mice. 0/p, non-/phosphorylation; u/s, un-/spliced *Xbp1*. Quantitation of IRE1α and the ratio of spliced to total *Xbp1* shown below the gel as mean (n = 4-5 mice per group). **(B)** Western blot analysis of ER chaperones GRP94, BiP and PDI from the cerebellum of 5-week-old mice with quantitation shown below the gel as mean (n = 4-6 mice per group). **(C-D)** Representative TEM images of Purkinje cells (outlined by red dotted lines) of 3- (**C**) and 24- (**D**) week-old mice. N, nucleus; M, mitochondria. n = 2 mice each genotype at each age.

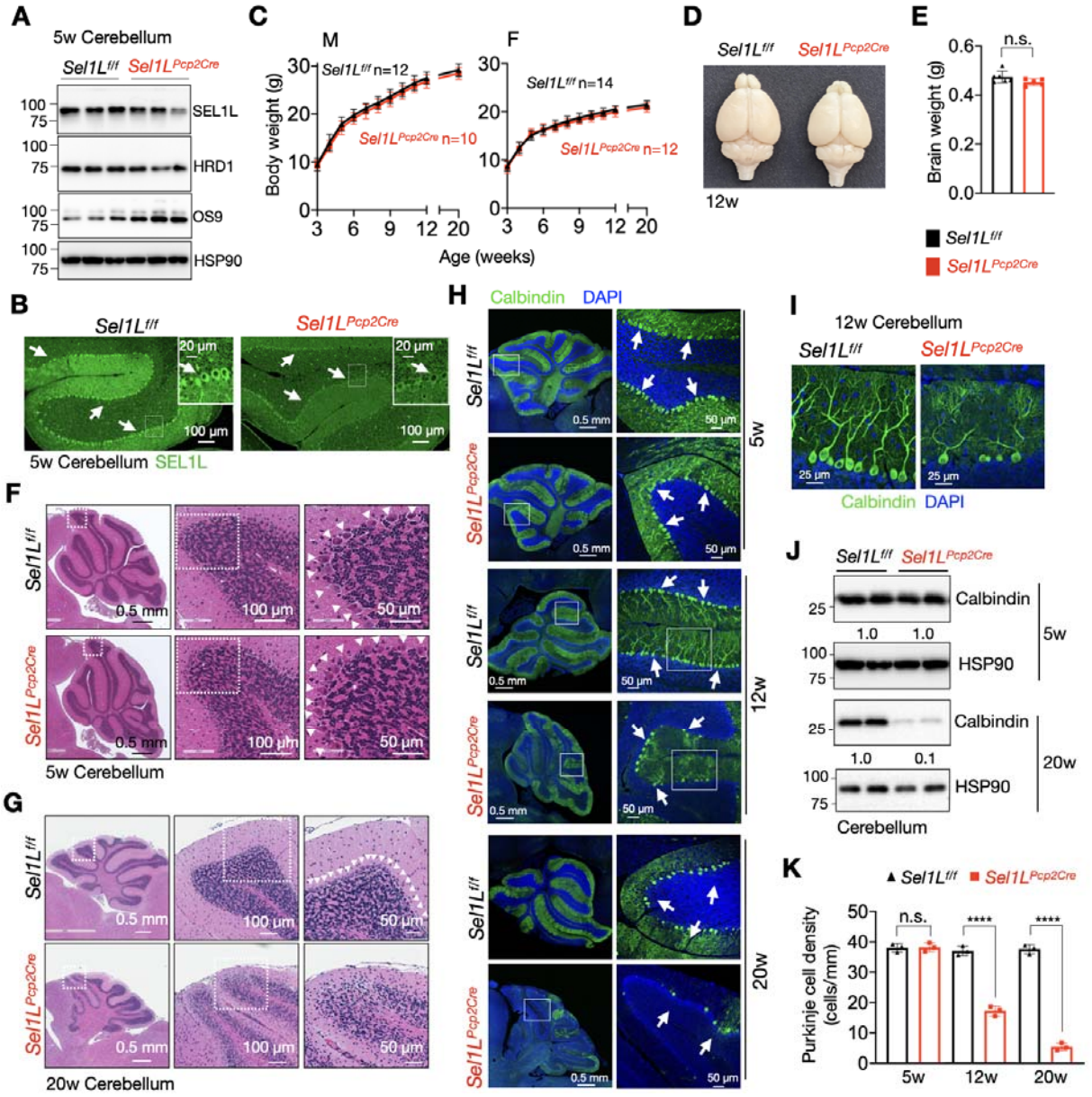

Fig. 6. Purkinje cell SEL1L deletion leads to progressive Purkinje cell loss.
(A) Western blot analysis of the cerebellum of 5-week-old mice with quantitation shown in fig. S3A (n = 3 mice per group). **(B)** Representative confocal images of SEL1L (green) staining in the cerebellum of 5-week-old mice (n = 3 mice per group). **(C)** Body weight (n = 10-14 mice per group). **(D-E)** Representative pictures of brains from 12-week-old mice with quantitation of brain weight in (**E**) (n = 5-6 mice per group). **(F-G)** Hematoxylin & eosin (H&E) stained sagittal sections of the cerebellum from 5- (**F**) and 20- (**G**) week-old mice. White arrowheads, Purkinje cells (n = 3 mice per group). **(H-I)** Representative confocal images of Calbindin (green) staining in the cerebellum of 5-,12- and 20-week-old mice. White arrows, Purkinje cells. The boxed areas of 12-week-old cerebellum are shown in (**I**) (n = 3 mice per group). **(J)** Western blot analysis of Calbindin in the cerebellum of 5-week-old mice with quantitation shown below the gel as mean (n = 2 mice per group). **(K)** Quantitation of Purkinje cell density in H&E-stained sagittal sections of the cerebellum of mice at 5, 12, and 20 weeks of age (n = 3 mice per group). Data are presented as mean ±SEM. n.s., not significant; ****p<0.0001 by one-way ANOVA followed by Tukey's post hoc test (K).

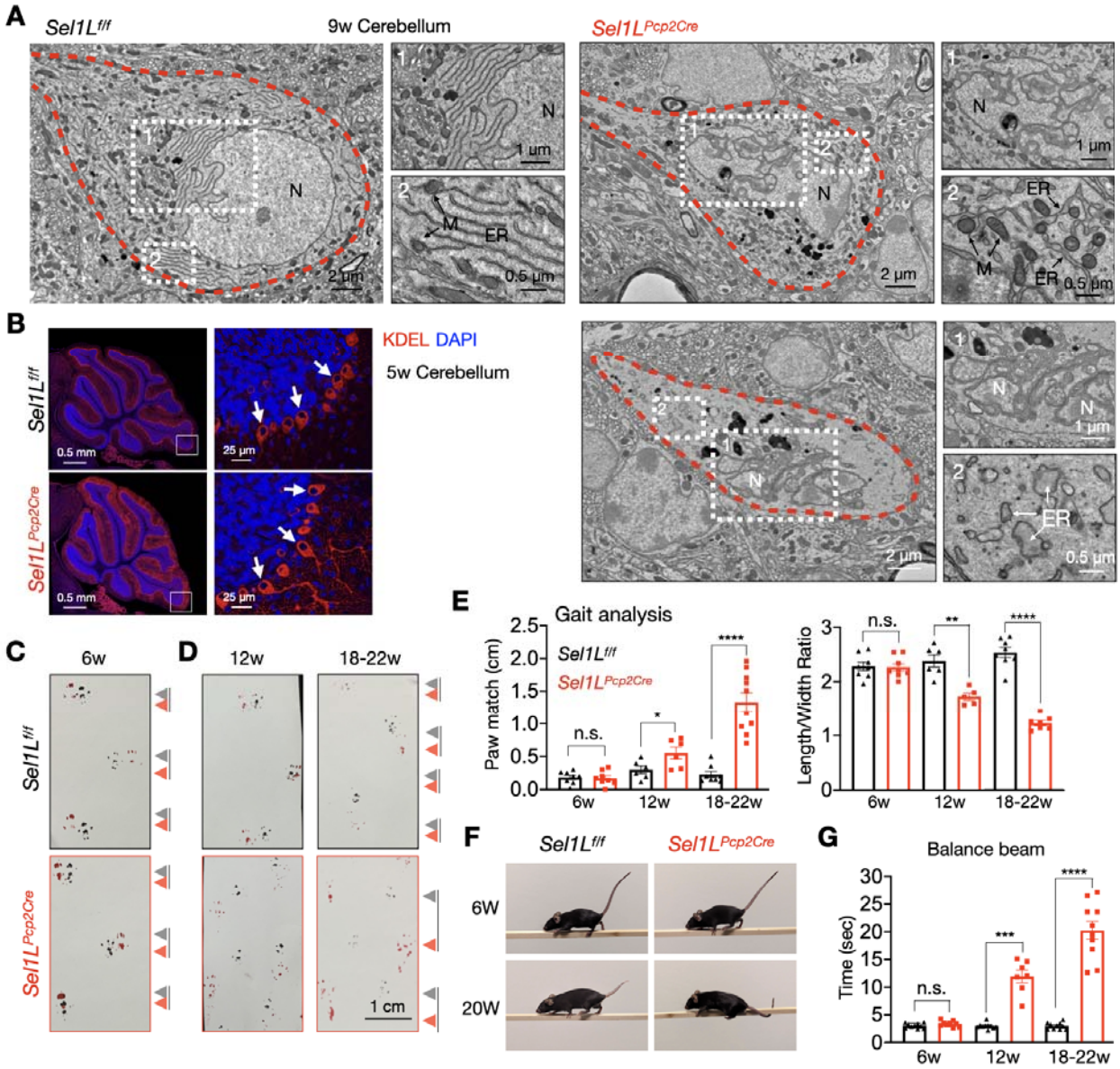

Fig. 7. Purkinje cell-specific SEL1L deletion leads to progressive cell death and cerebellar ataxia. **(A)** Representative TEM images of Purkinje cells (outlined by red dotted lines) from 9-week-old mice. N, nucleus; M, mitochondria (n = 2 mice each). **(B)** Representative confocal images of KDEL (red) in the cerebellum of 5-week-old mice. White arrows, Purkinje cells (n = 3 per group). **(C)** Representative pictures of paw prints from 6-week-old mice showing normal gait. The grey and red arrows indicate forelimb and hindlimb, respectively; and the lines between grey and red arrow indicate the distance between the two limbs. **(D)** Representative pictures of paw prints showing impaired gait in 12- and 18-22-week-old KO mice. **(E)** Quantitation of gait analysis from 6 to 22-week-old littermates of both genders (n = 6-10 mice per group). **(F)** Representative pictures of balance beam test from 6 and 20-week-old mice. **(G)** Quantification of balance beam test from mice at 6, 12 and18-22 weeks of age (n = 7-10 mice per group). Data are presented as mean ± SEM. n.s., not significant. *p<0.05, **p<0.01, ***p<0.001 and ****p<0.0001 by one-way ANOVA followed by Tukey's post hoc test (E, G).

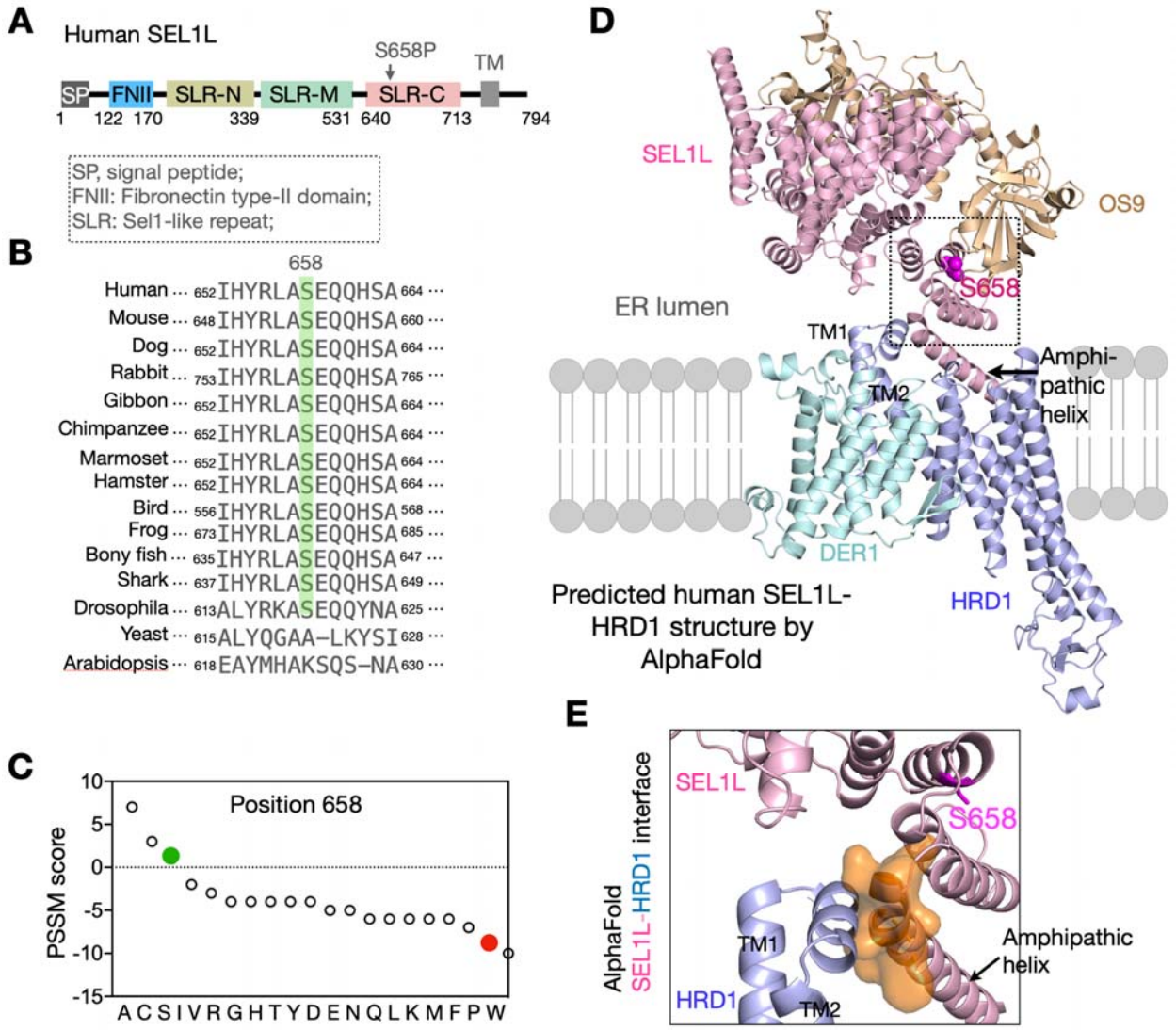

Fig. 8. Sequence and structural analyses of S658P SEL1L.
(A) Schematic diagram of human SEL1L with the location of the variant indicated. SP, signal peptide; FNII, fibronectin type II domain; SLR-N/M/C, Sel1-like repeats at N-, Middle- and C-terminal; TM, transmembrane. **(B)** Amino acid sequence alignment of SEL1L showing the conservation of SEL1L S658 residue across species (highlighted in green). **(C)** Position-specific scoring matrix (PSSM) scores for amino acid position in SEL1L, with WT in green and variant in red. **(D)** Structural prediction of human SEL1L/OS9/HRD1/DERLIN ERAD complex using AlphaFold2 with SEL1L S658 shown in pink atoms. The arrow indicates the Amphipathic helix which interacts with HRD1. **(E)** Side view of a space-filling model of the HRD1-SEL1L interface containing TMs1-2 of HRD1 and amphipathic helix of SEL1L.

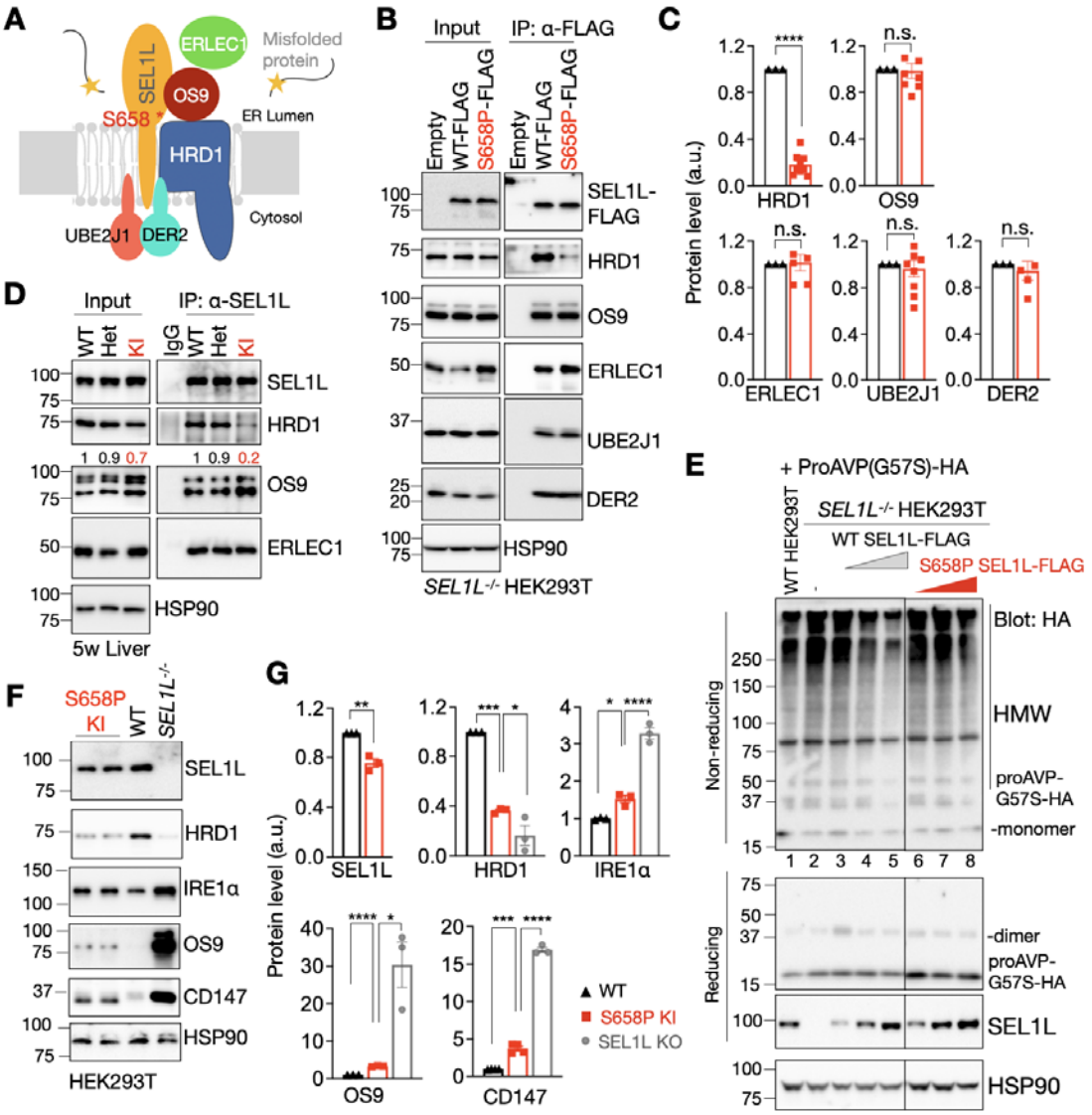

Fig. 9. *SEL1L* S658P is a hypomorphic variant and attenuates its interaction with HRD1. **(A)** Diagram for the protein components of SEL1L-HRD1 ERAD complex. **(B-C)** Immunoprecipitation of FLAG-agarose in *SEL1L*$^{-/-}$ HEK293T cells transfected with indicated SEL1L-FLAG constructs to examine their interactions with other ERAD components, with quantitation of SEL1L with indicated proteins shown in (**C**) (n = 4-9 independent samples per genotype). **(D)** Immunoprecipitation of SEL1L in 5-week-old liver to examine the endogenous SEL1L interaction with other ERAD components (two independent repeats). **(E)** Reducing and non-reducing SDS-PAGE and Western blot analyses of proAVP-G57S high molecular-weight (HMW) aggregates in WT or *SEL1L*$^{-/-}$ HEK293T cells transfected with indicated SEL1L-FLAG constructs in a dose-dependent manner, with quantitation of proAVP-G57S-HA HMW shown in fig. S6C. Two panels were from the same experiment with the irrelevant lanes in the middle cut off (n = 7 and 4 independent samples for WT and S658P SEL1L-FLAG). **(F-G)** Western blot analysis of ERAD complex and its substrates in WT or SEL1L S658P knock-in (KI) HEK293T cells, with quantitation shown in (**G**) (n = 3-4 independent samples per genotype). Data are presented as mean ± SEM. n.s., not significant. **p<0.01, ***p<0.001 and ****p<0.0001 by two-tailed Student's *t*-test (C, G:OS9) and one-way ANOVA followed by Tukey's post hoc test (G).

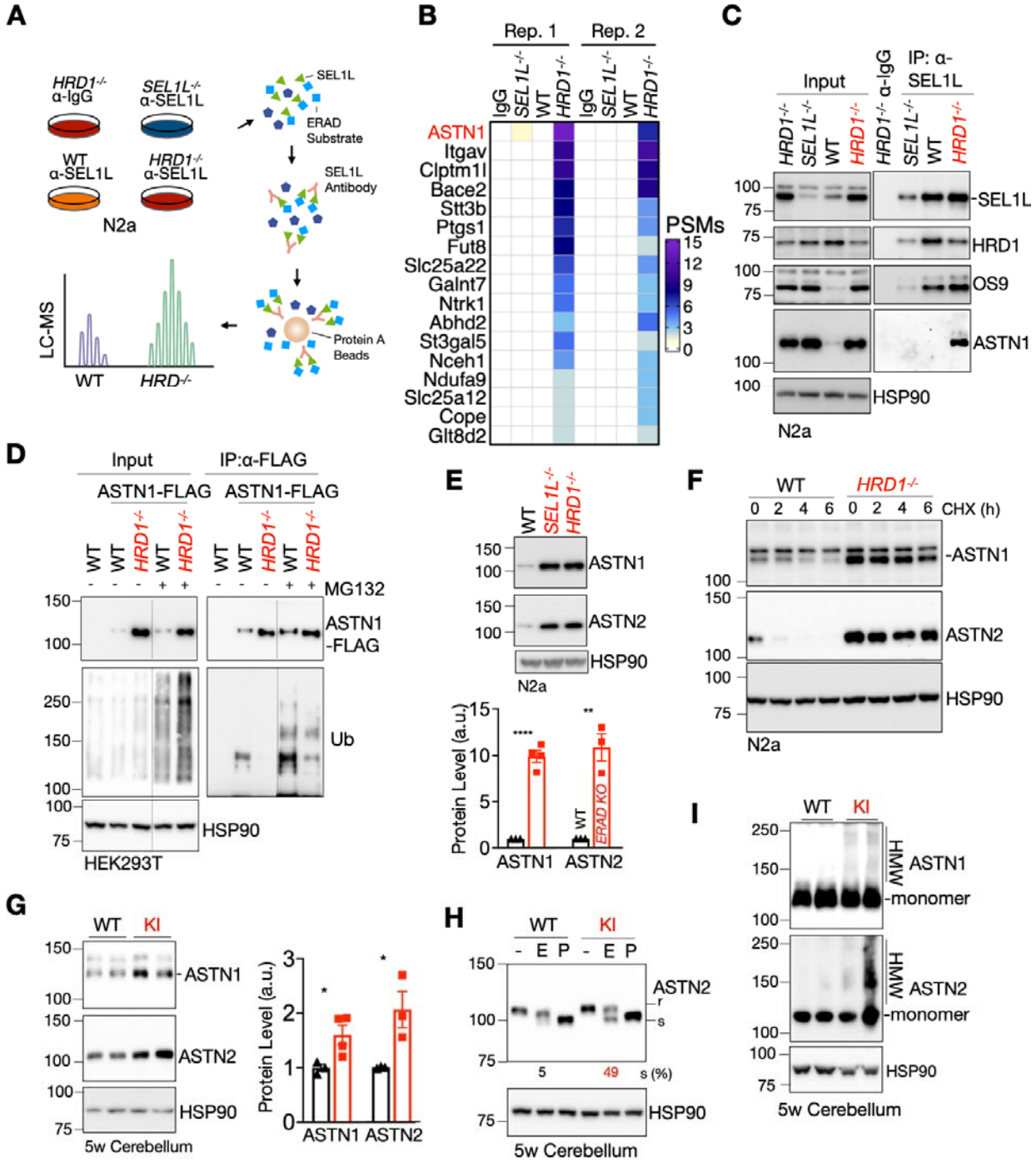

Fig. 10. Identification of ASTN1/2 as endogenous ERAD substrates

(A) The workflow of mass spectrometric analysis of SEL1L interactome in WT, *SEL1L*$^{-/-}$ or *HRD1*$^{-/-}$ N2a cells. **(B)** Heatmap showing the top hits ranked by mean PSM counts in *HRD1*$^{-/-}$ N2a from two independent experiments. **(C)** Immunoprecipitation of SEL1L in WT, *SEL1L*$^{-/-}$ or *HRD1*$^{-/-}$ N2a cells to examine the interaction between SEL1L and ASTN1 (two repeats). **(D)** Immunoprecipitation of FLAG-agarose in ASTN1-FLAG -transfected WT, *SEL1L*$^{-/-}$ or *HRD1*$^{-/-}$ HEK293T cells treated with or without MG132 to measure ASTN1 ubiquitination (two repeats). Two panels were from the same experiment, with the irrelevant middle lanes cut off. **(E)** Western blot analysis of ASTN1 and ASTN2 proteins in WT,

SEL1L$^{-/-}$ or *HRD1*$^{-/-}$ N2a cells with quantitation shown below (n = 3-4 individual samples per group). **(F)** Cycloheximide (CHX) analysis of ASTN1 and ASTN2 proteins in WT or *HRD1*$^{-/-}$ N2a cells with quantitation shown in fig. S7G (n = 3-8 individual samples per group). *SEL1L*$^{-/-}$ or *HRD1*$^{-/-}$ N2a cells were included as a control as "ERAD KO". **(G)** Western blot analysis of ASTN1 and ASTN2 proteins in the cerebellum of 5-week-old mice with quantitation shown on the right (n = 3-4 individual samples per group). **(H)** Western blot analysis in the cerebellum of 5-week-old mice treated with Endo H (E) or PNGase F (P) with quantitation of percent of EndoH-sensitive (s) form as mean from two experiments shown below. r, EndoH resistant. **(I)** Non-reducing SDS-PAGE followed by Western blot analysis of ASTN1 and ASTN2 proteins in the cerebellum to visualize the formation of HMW complexes in the cerebellum of KI mice. Data are mean ± SEM. *$p<0.05$, **$p<0.01$ and ****$p<0.0001$ by two-tailed Student's *t*-test (E, G).

FIGURE LEGENDS

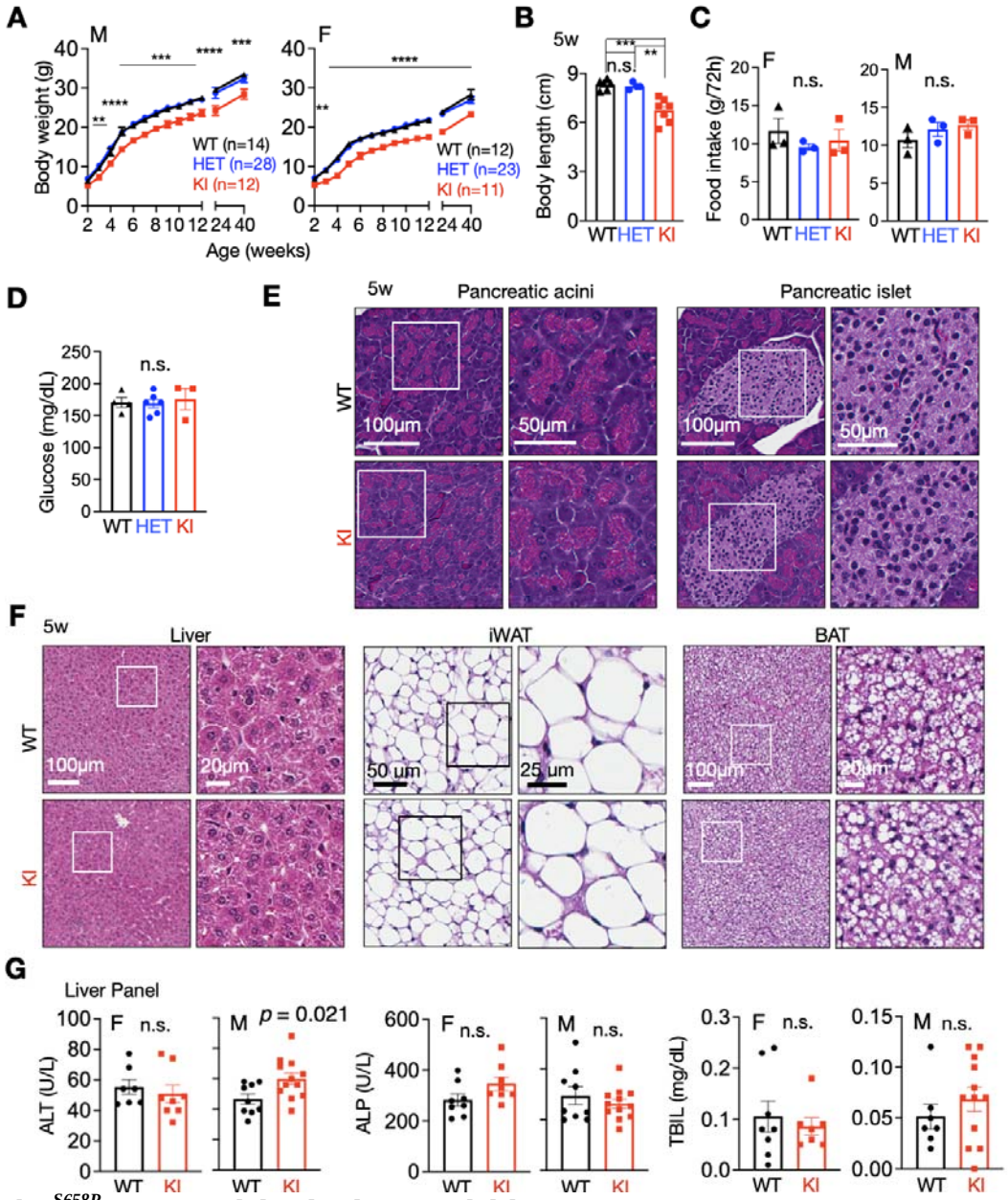

Fig. 1. *Sel1L*^{S658P} KI mice exhibit developmental delay.

(A) Growth curve. n = 11-28 mice for male and n = 11-23 mice for female per group. **(B)** Body length of 5-week-old mice of both genders (n = 4-7 mice per group). **(C)** 72 hr food intake of 5-week-old mice of both genders (n = 3 mice per group). n.s. is comparing all the groups. **(D)** Ad libitum blood glucose levels of 5-week-old mice (n = 3-6 mice per group). n.s. is comparing all the groups. **(E-F)** Hematoxylin & eosin (H&E) images of various peripheral tissues (**E**, pancreatic acini and islet; **F**, Liver, iWAT and BAT) from 5-week-old mice (n = 3 mice per group). iWAT, inguinal white adipose tissue; BAT, brown adipose tissue. **(G)** Serum levels of alanine transaminase (ALT), total bilirubin (TBIL) and alkaline phosphatase (ALP) in 5-week-old mice of both sexes (n = 7-12 mice per group). Data are presented as mean ± SEM. n.s., not significant; **p<0.01, ***p<0.001 and ****p<0.0001 by two-way ANOVA followed by Tukey's multiple comparisons test for each age (A), one-way ANOVA followed by Tukey's post hoc test (B) and two-tailed Student's *t*-test (G).

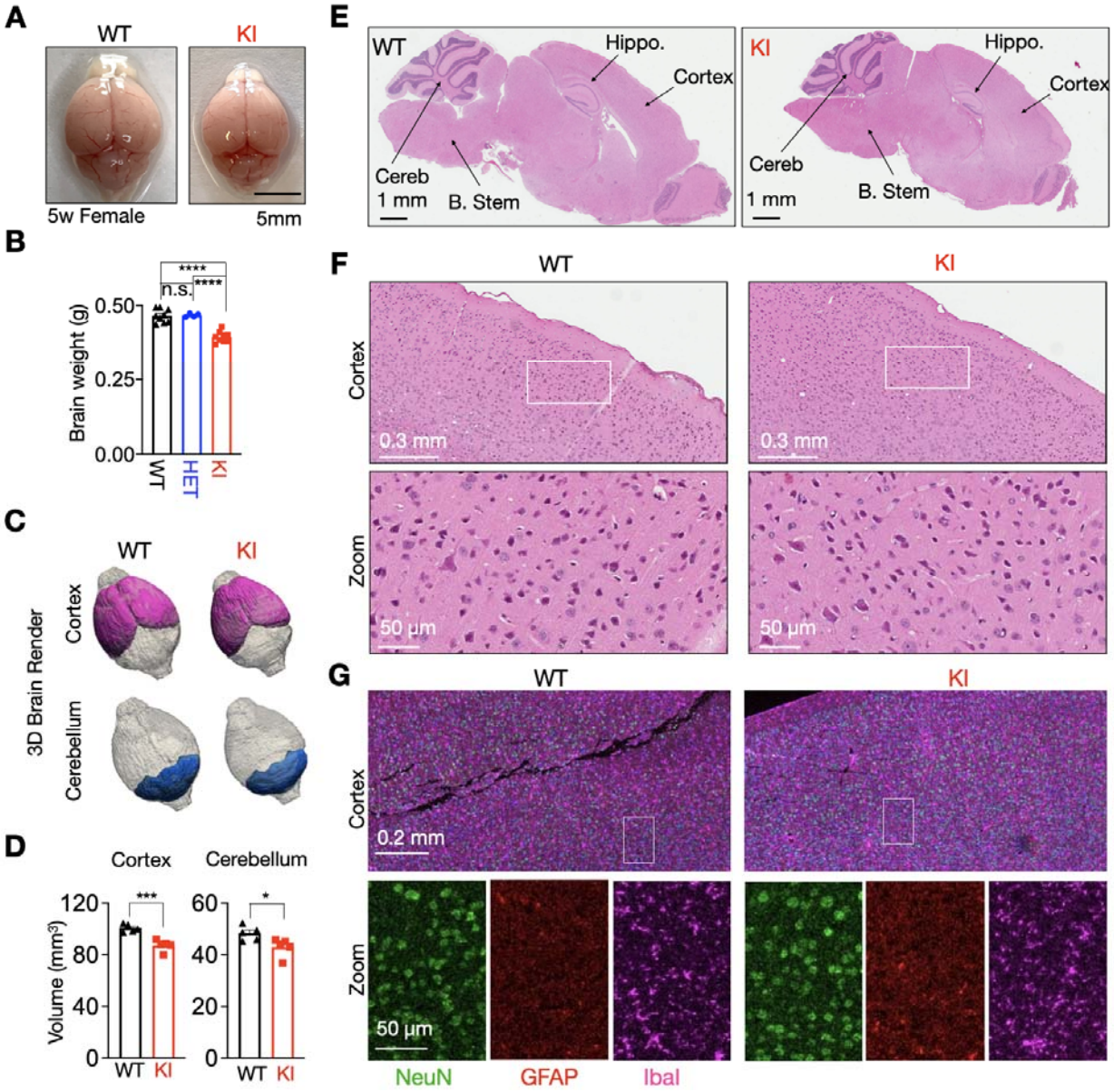

Fig. 2. *Sel1L*^{S658P} KI mice exhibit microcephaly.
(A-B) Representative pictures of brains from 5-week-old mice, with quantitation of brain weight shown in (**B**) (n = 9, 4 and 9 mice for WT, HET and KI). **(C-D)** 3D rendering of cortex and cerebellum from 5-week-old mice, with quantitation shown in (**D**) (n = 5 mice per group). **(E-F)** Hematoxylin & eosin (H&E) stained sagittal sections of whole brain (**E**) and cortex (**F**) from 5-week-old mice (n = 3 mice per group). Hippo., hippocampus; B. Stem, brain stem; Cereb., cerebellum. **(G)** Representative confocal images of NeuN (green), GFAP (red) and Iba1 (purple) for neurons, astrocytes and microglia in the brains of 5-week-old mice (n = 2 mice per group). Staining of the whole brain is shown in (Fig. S2B). "Data are presented as mean ± SEM. n.s., not significant; *p<0.05, ***p<0.001 and ****p<0.0001 by one-way ANOVA followed by Tukey's post hoc test (B) and two-tailed Student's *t*-test (D).

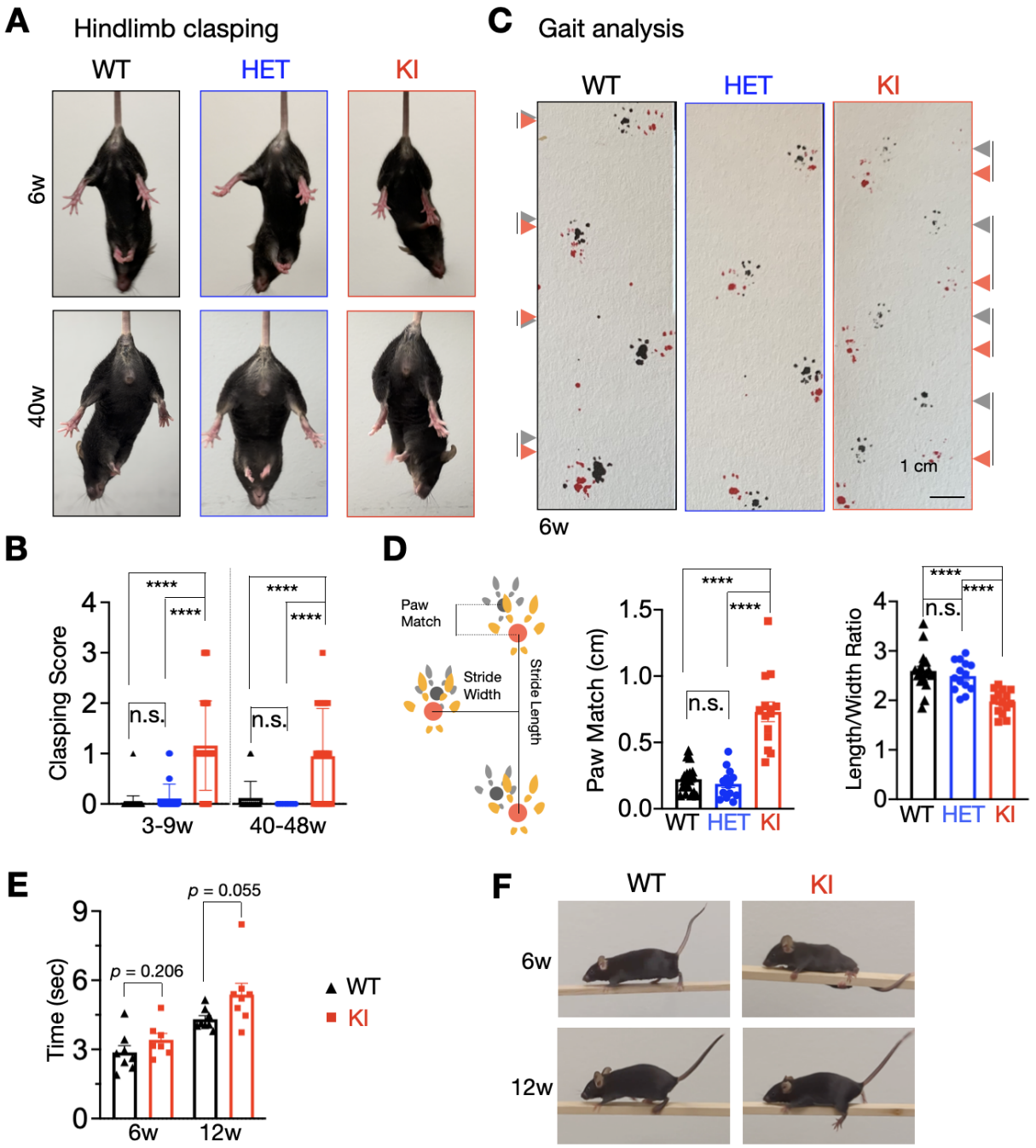

Fig. 3. *Sel1L*^{S658P} KI mice exhibit early-onset, non-progressive, mild ataxia.
(A-B) Representative pictures of hindlimb clasping (**A**) and score quantitation (**B**) of 3-9 (n = 49, 51 and 38 for WT, HET and KI) and 40-48 (n = 17, 8 and 20 mice for WT, HET and KI) -week-old littermates of both genders. **(C-D)** Representative pictures (**C**), cartoon schematic of paw prints (left, **D**) and quantitation of gait analysis (right, **D**) of 6-week-old littermates of both genders. The grey and red arrows in (**C**) indicate forelimb and hindlimb, respectively; and the lines between grey and red arrow indicate the distance between the two limbs (n = 14-18 mice per group). **(E)** Quantification of balance beam test from mice at 6 and 12 weeks of age (n = 7-8 per group). **(F)** Representative pictures of slips of 6 and 12-week-old KI mice on balance beam. **(G)** Data are presented as mean ± SEM. n.s., not significant. ****p<0.0001 by one-way ANOVA followed by Tukey's post hoc test (B, D) and two-tailed Student's *t*-test (E).

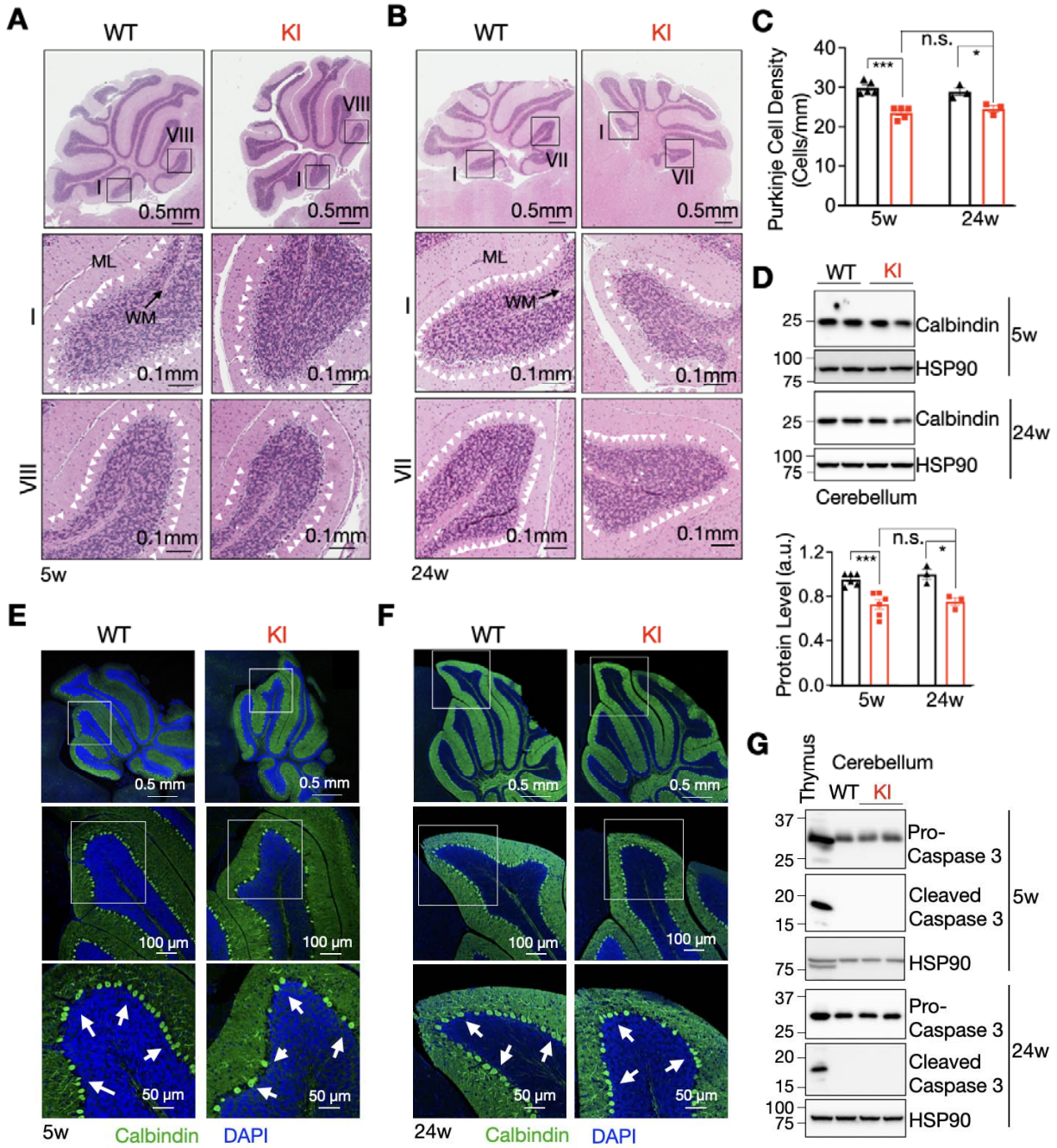

Fig. 4. *Sel1L*^{S658P} KI mice exhibit an early onset, non-progressive, mild reduction of Purkinje cells. **(A-C)** Hematoxylin & eosin (H&E) stained sagittal sections of the cerebellum from 5- (**A**) and 24- (**B**) week-old mice, with quantitation of Purkinje cell density shown in (**C**) (n = 3-5 mice per group). White arrowheads, Purkinje cells. ML, molecular layer; MW, white matter. **(D)** Western blot analysis of cerebellum of 5- and 24-week-old mice with quantitation shown below (n = 3-6 mice per group). **(E-F)** Representative confocal images of Calbindin (green) in the cerebellum of 5- (**E**) and 24- (**F**) week-old mice. White arrows, Purkinje cells (n = 3 mice per group). **(G)** Western blot analysis of cell death in the cerebellum of 5- and 24-week-old mice. The thymus, a positive control (n = 2 mice per group). Data are presented as mean ± SEM. n.s., not significant. *p<0.05 and ***p<0.001 by two-tailed Student's *t*-test (C, D).

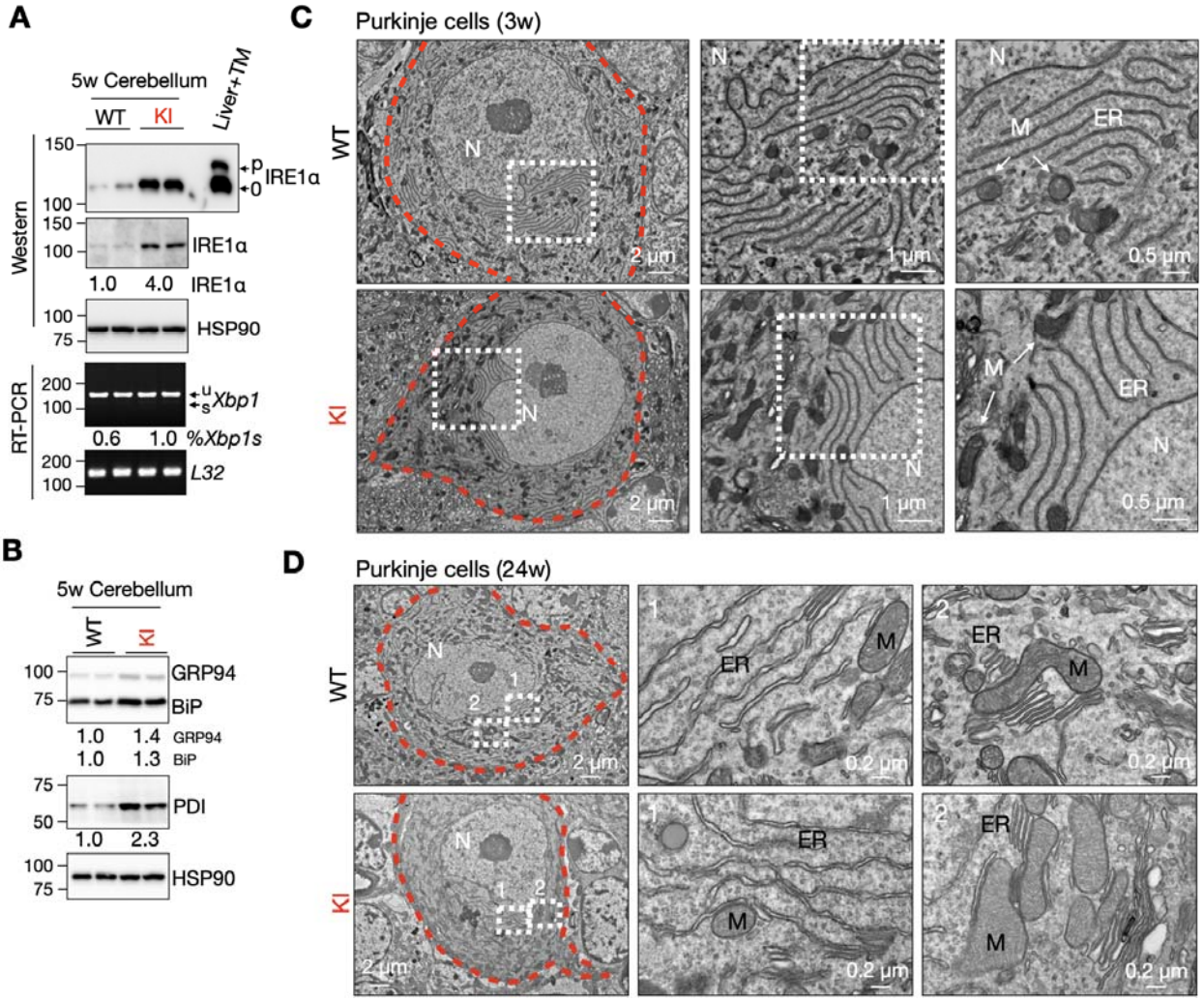

Fig. 5. Subtle alteration of ER homeostasis in the cerebellum of *Sel1L*^{S658P} KI mice.
(A) Western blot analysis of IRE1α phosphorylation (top) and RT-PCR of *Xbp1* splicing in the cerebellum of 5-week-old mice. 0/p, non-/phosphorylation; u/s, un-/spliced *Xbp1*. Quantitation of IRE1α and the ratio of spliced to total *Xbp1* shown below the gel as mean (n = 4-5 mice per group). **(B)** Western blot analysis of ER chaperones GRP94, BiP and PDI from the cerebellum of 5-week-old mice with quantitation shown below the gel as mean (n = 4-6 mice per group). **(C-D)** Representative TEM images of Purkinje cells (outlined by red dotted lines) of 3- (**C**) and 24- (**D**) week-old mice. N, nucleus; M, mitochondria. n = 2 mice each genotype at each age.

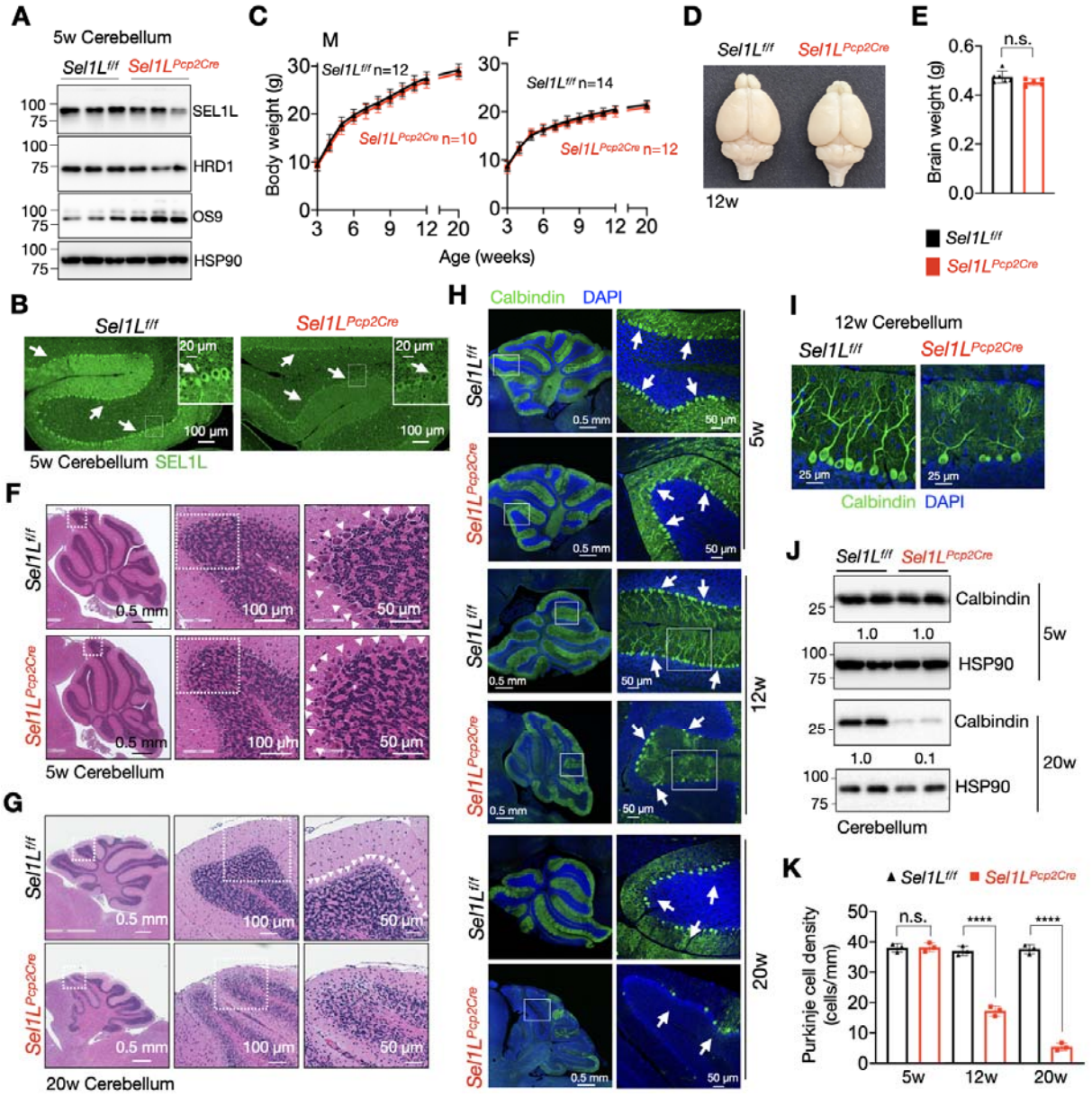

Fig. 6. Purkinje cell SEL1L deletion leads to progressive Purkinje cell loss.
(A) Western blot analysis of the cerebellum of 5-week-old mice with quantitation shown in fig. S3A (n = 3 mice per group). **(B)** Representative confocal images of SEL1L (green) staining in the cerebellum of 5-week-old mice (n = 3 mice per group). **(C)** Body weight (n = 10-14 mice per group). **(D-E)** Representative pictures of brains from 12-week-old mice with quantitation of brain weight in (**E**) (n = 5-6 mice per group). **(F-G)** Hematoxylin & eosin (H&E) stained sagittal sections of the cerebellum from 5- (**F**) and 20- (**G**) week-old mice. White arrowheads, Purkinje cells (n = 3 mice per group). **(H-I)** Representative confocal images of Calbindin (green) staining in the cerebellum of 5-,12- and 20-week-old mice. White arrows, Purkinje cells. The boxed areas of 12-week-old cerebellum are shown in (**I**) (n = 3 mice per group). **(J)** Western blot analysis of Calbindin in the cerebellum of 5-week-old mice with quantitation shown below the gel as mean (n = 2 mice per group). **(K)** Quantitation of Purkinje cell density in H&E-stained sagittal sections of the cerebellum of mice at 5, 12, and 20 weeks of age (n = 3 mice per group). Data are presented as mean ±SEM. n.s., not significant; ****p<0.0001 by one-way ANOVA followed by Tukey's post hoc test (K).

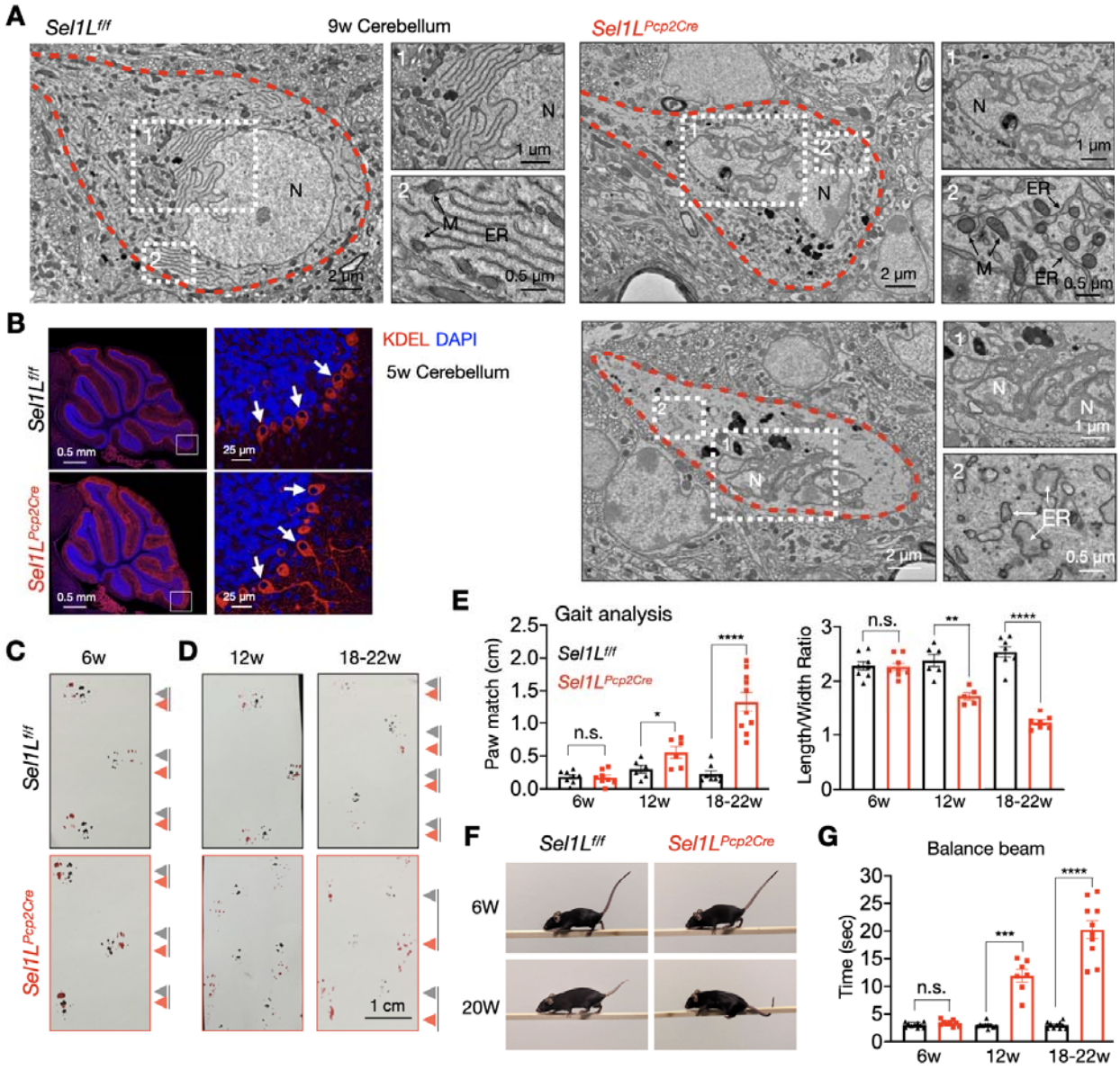

Fig. 7. Purkinje cell-specific SEL1L deletion leads to progressive cell death and cerebellar ataxia. **(A)** Representative TEM images of Purkinje cells (outlined by red dotted lines) from 9-week-old mice. N, nucleus; M, mitochondria (n = 2 mice each). **(B)** Representative confocal images of KDEL (red) in the cerebellum of 5-week-old mice. White arrows, Purkinje cells (n = 3 per group). **(C)** Representative pictures of paw prints from 6-week-old mice showing normal gait. The grey and red arrows indicate forelimb and hindlimb, respectively; and the lines between grey and red arrow indicate the distance between the two limbs. **(D)** Representative pictures of paw prints showing impaired gait in 12- and 18-22-week-old KO mice. **(E)** Quantitation of gait analysis from 6 to 22-week-old littermates of both genders (n = 6-10 mice per group). **(F)** Representative pictures of balance beam test from 6 and 20-week-old mice. **(G)** Quantification of balance beam test from mice at 6, 12 and18-22 weeks of age (n = 7-10 mice per group). Data are presented as mean ± SEM. n.s., not significant. *p<0.05, **p<0.01, ***p<0.001 and ****p<0.0001 by one-way ANOVA followed by Tukey's post hoc test (E, G).

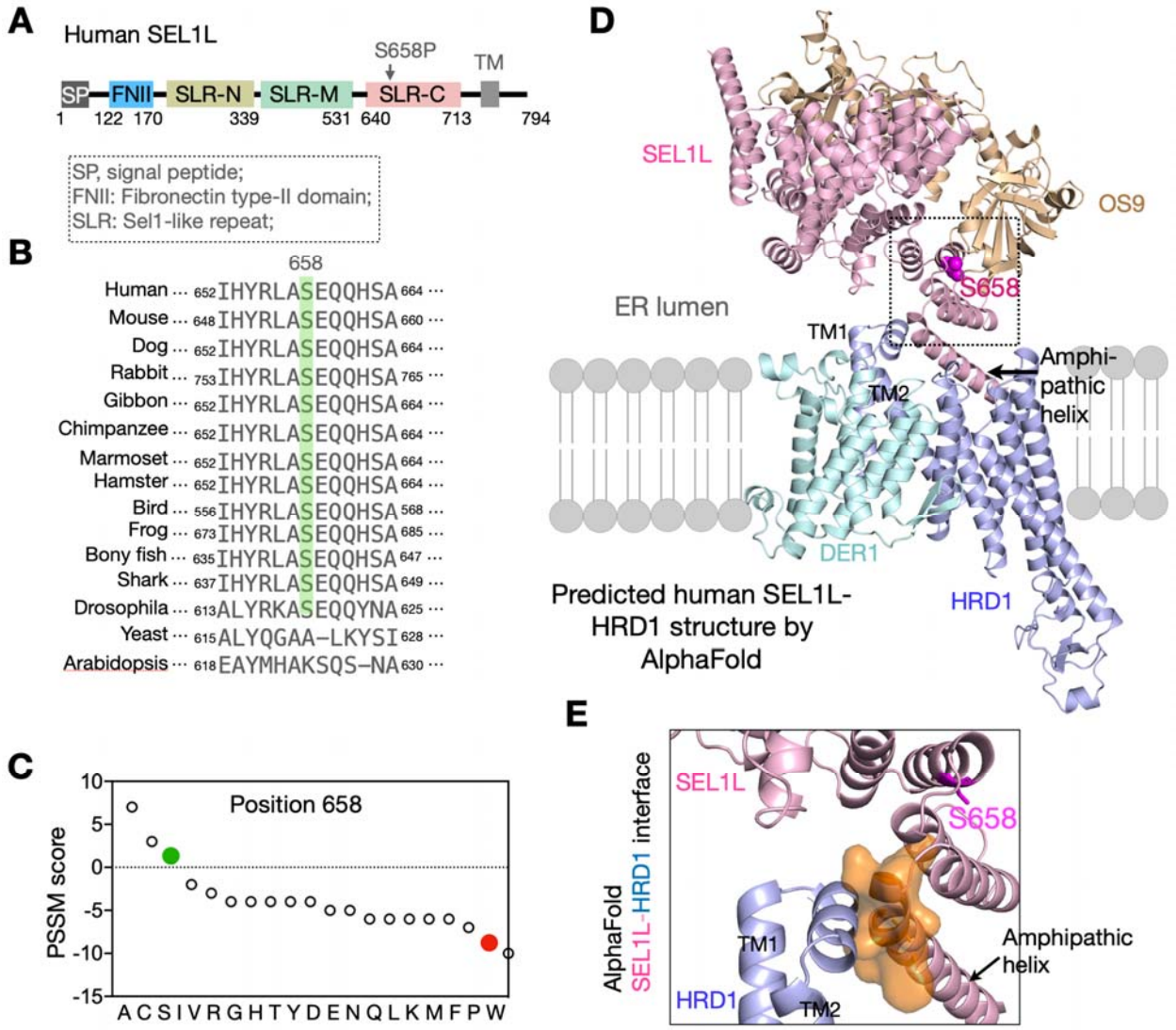

Fig. 8. Sequence and structural analyses of S658P SEL1L.
(A) Schematic diagram of human SEL1L with the location of the variant indicated. SP, signal peptide; FNII, fibronectin type II domain; SLR-N/M/C, Sel1-like repeats at N-, Middle- and C-terminal; TM, transmembrane. **(B)** Amino acid sequence alignment of SEL1L showing the conservation of SEL1L S658 residue across species (highlighted in green). **(C)** Position-specific scoring matrix (PSSM) scores for amino acid position in SEL1L, with WT in green and variant in red. **(D)** Structural prediction of human SEL1L/OS9/HRD1/DERLIN ERAD complex using AlphaFold2 with SEL1L S658 shown in pink atoms. The arrow indicates the Amphipathic helix which interacts with HRD1. **(E)** Side view of a space-filling model of the HRD1-SEL1L interface containing TMs1-2 of HRD1 and amphipathic helix of SEL1L.

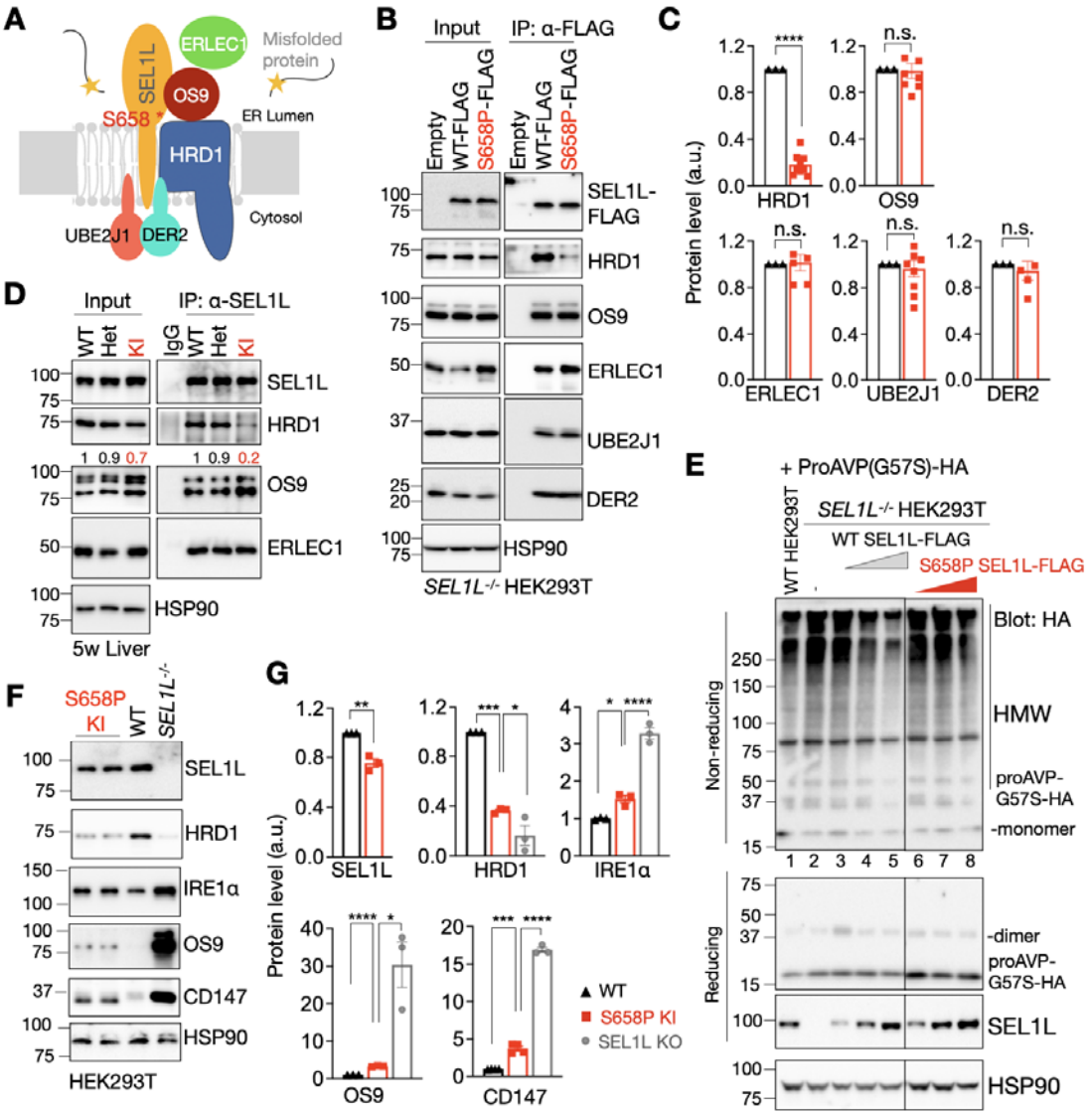

Fig. 9. *SEL1L* S658P is a hypomorphic variant and attenuates its interaction with HRD1. **(A)** Diagram for the protein components of SEL1L-HRD1 ERAD complex. **(B-C)** Immunoprecipitation of FLAG-agarose in *SEL1L*$^{-/-}$ HEK293T cells transfected with indicated SEL1L-FLAG constructs to examine their interactions with other ERAD components, with quantitation of SEL1L with indicated proteins shown in (**C**) (n = 4-9 independent samples per genotype). **(D)** Immunoprecipitation of SEL1L in 5-week-old liver to examine the endogenous SEL1L interaction with other ERAD components (two independent repeats). **(E)** Reducing and non-reducing SDS-PAGE and Western blot analyses of proAVP-G57S high molecular-weight (HMW) aggregates in WT or *SEL1L*$^{-/-}$ HEK293T cells transfected with indicated SEL1L-FLAG constructs in a dose-dependent manner, with quantitation of proAVP-G57S-HA HMW shown in fig. S6C. Two panels were from the same experiment with the irrelevant lanes in the middle cut off (n = 7 and 4 independent samples for WT and S658P SEL1L-FLAG). **(F-G)** Western blot analysis of ERAD complex and its substrates in WT or SEL1L S658P knock-in (KI) HEK293T cells, with quantitation shown in (**G**) (n = 3-4 independent samples per genotype). Data are presented as mean ± SEM. n.s., not significant. **p<0.01, ***p<0.001 and ****p<0.0001 by two-tailed Student's *t*-test (C, G:OS9) and one-way ANOVA followed by Tukey's post hoc test (G).

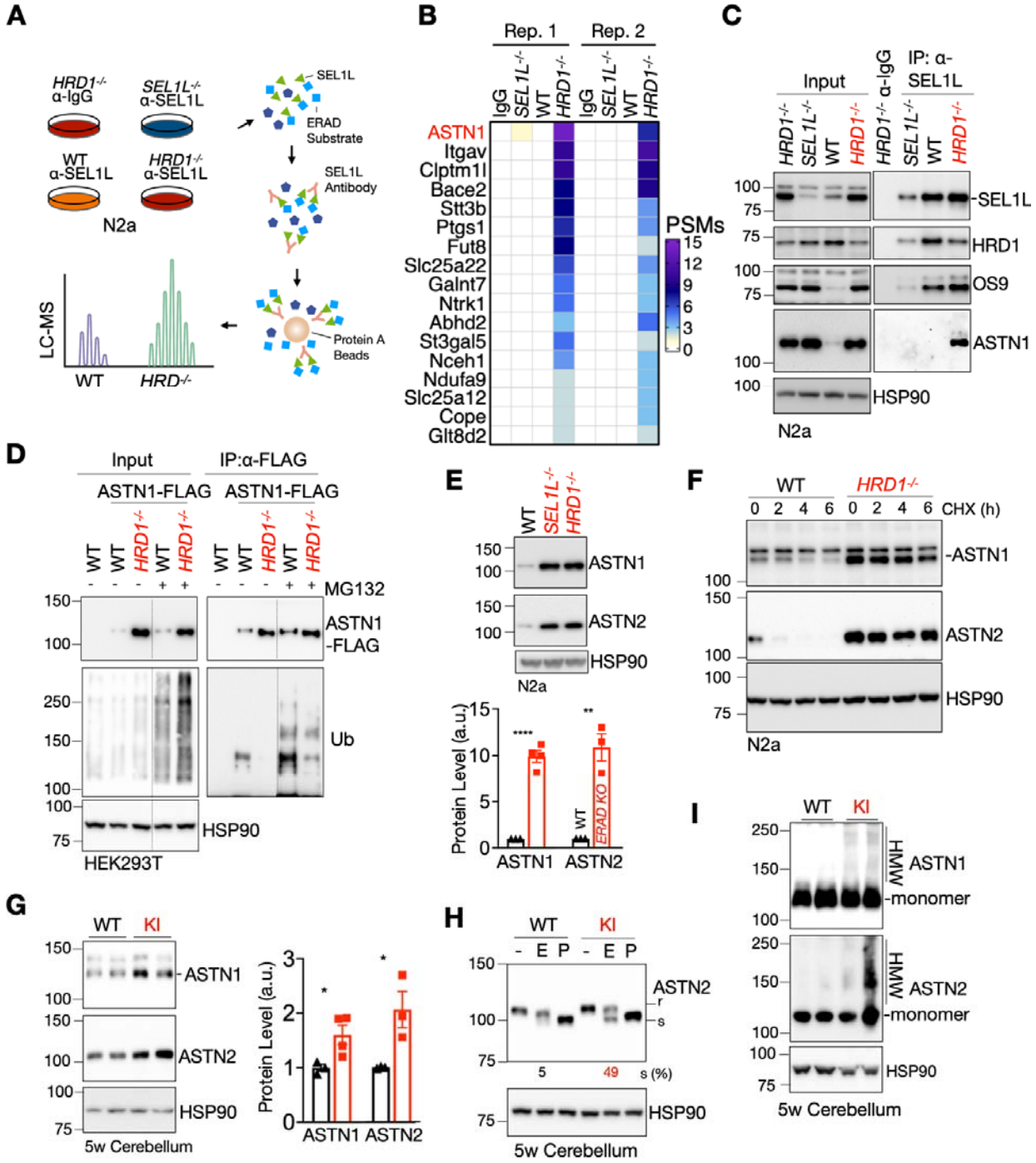

Fig. 10. Identification of ASTN1/2 as endogenous ERAD substrates

(A) The workflow of mass spectrometric analysis of SEL1L interactome in WT, *SEL1L*$^{-/-}$ or *HRD1*$^{-/-}$ N2a cells. **(B)** Heatmap showing the top hits ranked by mean PSM counts in *HRD1*$^{-/-}$ N2a from two independent experiments. **(C)** Immunoprecipitation of SEL1L in WT, *SEL1L*$^{-/-}$ or *HRD1*$^{-/-}$ N2a cells to examine the interaction between SEL1L and ASTN1 (two repeats). **(D)** Immunoprecipitation of FLAG-agarose in ASTN1-FLAG -transfected WT, *SEL1L*$^{-/-}$ or *HRD1*$^{-/-}$ HEK293T cells treated with or without MG132 to measure ASTN1 ubiquitination (two repeats). Two panels were from the same experiment, with the irrelevant middle lanes cut off. **(E)** Western blot analysis of ASTN1 and ASTN2 proteins in WT,

SEL1L$^{-/-}$ or *HRD1*$^{-/-}$ N2a cells with quantitation shown below (n = 3-4 individual samples per group). **(F)** Cycloheximide (CHX) analysis of ASTN1 and ASTN2 proteins in WT or *HRD1*$^{-/-}$ N2a cells with quantitation shown in fig. S7G (n = 3-8 individual samples per group). *SEL1L*$^{-/-}$ or *HRD1*$^{-/-}$ N2a cells were included as a control as "ERAD KO". **(G)** Western blot analysis of ASTN1 and ASTN2 proteins in the cerebellum of 5-week-old mice with quantitation shown on the right (n = 3-4 individual samples per group). **(H)** Western blot analysis in the cerebellum of 5-week-old mice treated with Endo H (E) or PNGase F (P) with quantitation of percent of EndoH-sensitive (s) form as mean from two experiments shown below. r, EndoH resistant. **(I)** Non-reducing SDS-PAGE followed by Western blot analysis of ASTN1 and ASTN2 proteins in the cerebellum to visualize the formation of HMW complexes in the cerebellum of KI mice. Data are mean ± SEM. *$p<0.05$, **$p<0.01$ and ****$p<0.0001$ by two-tailed Student's *t*-test (E, G).